Near-trapping effect of wave-cylinders interaction on pore water pressure and liquefaction around a cylinder array

Zaibin Lin[a], Dubravka Pokrajac [b], Yakun Guo [c], Chencong Liao[d], Tian Tang[e]

a. Now Centre for Mathematical Modelling and Flow Analysis, School of Computing, Mathematics and Digital Technology, Manchester Metropolitan University, Manchester, M1 5GD, United Kingdom
Formerly School of Engineering, University of Aberdeen, AB24 3UE, UK
Corresponding author: zaibin.lin@gmail.com,
b. School of Engineering, University of Aberdeen, AB24 3UE, UK
c. Faculty of Engineering and Informatics, University of Bradford, BD7 1DP, UK,
d. Collaborative Innovation Centre for Advanced Ship and Deep-Sea Exploration, State Key Laboratory of Ocean Engineering, Department of Civil Engineering, Shanghai Jiao Tong University, Shanghai, 200240, China
e. Bekaert Technology Centre, Bekaert Company, Zwevegem, Belgium

Abstract: The near-trapping effects on wave-induced dynamic seabed response and liquefaction close to a multi-cylinder foundation in storm wave conditions are examined. Momentary liquefaction near multi-cylinder structures is simulated using an integrated wave-structure-seabed interaction model. The proposed model is firstly validated for the case of interaction of wave and a four-cylinder structure, with a good agreement with available experimental measurements. The validated model is then applied to investigate the seabed response around a four-cylinder structure at 0° and 45° incident angles. The comparison of liquefaction potential around individual cylinders in an array shows that downstream cylinder is well protected from liquefaction by upstream cylinders. For a range of incident wave parameters, the comparison with the results for a single pile shows the amplification of pressure within the seabed induced by progressive wave. This phenomenon is similar to the near-trapping phenomenon of free surface elevation within a cylinder array.

Key words: Wave-Structure-Seabed Interaction (WSSI); seabed response; four-cylinder foundation; near-trapping phenomenon; momentary liquefaction

1. Introduction

Multi-cylinder structures, one of the most common offshore foundations, are vulnerable to environmental impact of waves and currents, and the associated dynamic seabed response. The wave-induced run-up, forcing, and seabed instability around foundations may result in the collapse of offshore structures. For the critical centre-to-centre spacing between cylinders and a given range of incident wave numbers, the near-trapping phenomenon can occur within an array of cylinder (Ohl et al., 2001a). This phenomenon causes the local amplification of wave amplitude, which occurs due to the trapping of undisturbed incident wave inside an array of cylinders. As a result, the wave-induced run-up and forcing, as well as the associated seabed response in the vicinity of multi-cylinder foundation can be significantly greater than in the case of single cylinder (Kamath et al., 2016). The effect of these phenomena on the safety of offshore structures and their foundations is of particular interest and important due to the increasing applications of multi-cylinder foundations in offshore engineering.

Near-trapping phenomenon is a dominant factor considered in the design of sufficient air gap under the deck of offshore structures. This phenomenon has been systematically and intensively investigated by numerous researchers. To obtain the velocity potential surrounding the various arrangements of two cylinders and force components induced by linear water waves, Spring and Monkmeyer (1974) analytically solved the potential theory formulations using a direct matrix solution and multiple scattering (Twersky, 1952). Based on the same assumption used in Spring and Monkmeyer (1974), Linton and Evans (1990) simplified the theory, and proposed new formulae to estimate the free surface elevation around an array of cylinders, together with new formulae to calculate the first and second-order mean forces. Using eigenfunction expansions and an integral representation, Malenica et al. (1999) introduced a semi-analytical approach to solve for velocity potential with an incident monochromatic wave for estimating the second-order wave diffraction in the vicinity of an array of circular cylinders. The experimental investigations of the near-trapping phenomenon under regular and irregular incident waves with two incident wave directions are analysed by Ohl et al. (2001a; b) who pointed out that Malenica et al. (1999) overestimated the second order amplitude under the regular wave with 45° heading.

The rapid development of computing resources and techniques of Computational Fluid Dynamics (CFD) has made the full scale three-dimensional (3D) simulation of wave-structure interaction in ocean/offshore engineering problems possible. Extensive investigations were carried out to study these problems. An open source CFD model, REEF3D, was developed to investigate fully nonlinear wave-structure interaction with various arrangements of cylinder groups, including two cylinders in tandem (Kamath et al., 2015; Bihs et al., 2016) and four cylinders in an array (Kamath et al., 2016). In REEF3D continuity equations and Reynolds-averaged Navier-Stokes (RANS) equations, together with k-ω turbulence model are discretised using Finite Difference Method (FDM). The free surface between water and air is tracked by Level Set Method (LSM). In the study of Kamath et al. (2016), a pronounced amplification of the wave force on upstream cylinder was found by comparing the simulated results for the cases with and without the downstream cylinders in a four-cylinder array. Another broadly adopted open access CFD code in coastal/offshore engineering is the OpenFOAM with free C++ library for solving a wide range of fluid flow and solid mechanics problems using Finite Volume Method (FVM). With the help of the open source wave generation tool waves2Foam (Jacobsen et al., 2012) in OpenFOAM and the application of a slip boundary condition on the cylinder surface, Paulsen et al. (2014b) performed the intensive investigations of the fully nonlinear wave-cylinder interaction for a range of Keulegan–Carpenter (KC) numbers ($KC = U_{z=0}T/D$, where $U_{z=0}$ is the velocity amplitude at z=0 with z pointing vertically, T is wave period, and D is the diameter of cylinder, Sumer and Fredsøe 2006). By analysing the numerical results, it was concluded that the process of return flow from the back of cylinder and the passage of the wave crest made the dominant contributions to the occurrence of secondary load cycle. For the purpose of more efficient computation, Paulsen et al. (2014a) proposed an innovative and fully nonlinear domain decomposition approach, which involves coupling potential flow theory model (OceanWave3D, Engsig-Karup et al., 2009) and waves2Foam library. The good agreement between numerical and experimental results for irregular waves has demonstrated the accuracy and applicability of the coupled model. Chen et al. (2014) also elaborated a comprehensive study for exploring the applicability and capacity of OpenFOAM in evaluating fully nonlinear wave-cylinder interaction under regular and focused waves. Moreover, both wave generation and active absorbing boundaries were developed in Higuera et al. (2013a) (IHFOAM) for simulating wave-induced coastal engineering processes (Higuera et al., 2013b), and wave interaction with porous structures (Higuera et al., 2014a; Higuera et al., 2014b). A new moving boundary decomposed into multi-paddles and an enhanced active wave absorption boundary were integrated into IHFOAM (Higuera et al., 2015). All aforementioned research has been mainly concerned with wave interaction with coastal/offshore structures. However, the attention should also be paid to another important issue, namely the wave induced dynamic response in a porous seabed which occurs as a result of fully nonlinear wave-structure interactions.

Seabed stability in the vicinity of coastal/offshore structures is one of the most important issues in engineering design (Sumer and Fredsøe, 2002; Jeng, 2013; Sumer, 2014; Jeng, 2018). At the early stage of seabed stability research, analytical approximations on the basis of poro-elastic Biot's theory (Biot, 1941) were extensively used for investigating wave-induced seabed response. A considerable amount of both the theoretical and experimental porous seabed research before 2003 has been reviewed and summarized in Jeng (2003). In recent years, the applicability of three different soil models, including fully dynamic (FD), partially dynamic (PD), and quasi-static (QS) model, was investigated in Ulker and Rahman (2009) and Ulker et al. (2009). Their conclusions are consistent with Jeng and Cha (2003), who showed that the maximum discrepancy between the calculated results is within 3%. and they proposed the applicability for the three above-mentioned models in partially/fully saturated porous seabed. Considering the combined effect of current and nonlinear wave, Liao et al. (2013) proposed an analytical approximation to investigate the soil response within a porous seabed, and concluded that this effect had a considerable impact in the upper zone beneath seabed surface. However, due to underlying assumptions and simplifications these analytical approximations are not able to fully describe the complicated process of wave-induced seabed stability in the proximity of coastal/offshore structures.

Due to its practical importance and engineering applications, extensive laboratory experimental modelling studies have been conducted to investigate wave-induced soil response in a porous seabed. To understand the mechanism of pore water pressure and scour around a mono-pile foundation, Qi and Gao (2014) performed experimental studies with various combined wave and current parameters. Liu et al. (2015) conducted laboratory experiment in a one-dimensional (1-D) soil column to examine the pore pressure development under sinusoidal wave pressure applied at one end of the column. The thickness of sandy deposit was slightly reduced after a long-term dynamic wave loading. The oscillatory excess pore pressure within a well-mixed seabed, consisting of silt and sand, and the influence of the ratio of sand/silt in mixture were experimentally studied by Zhang et al. (2016) with a series of incident waves. Recently, Sun et al. (2019) conducted laboratory experiments to investigate the dynamic soil response and liquefaction potential around a buried pipeline in a trench layer. In the context of wave-induced soil response, the experimental studies have the capacity of directly capturing the realistic behaviour. However, the scope of physical experiments is limited by scale-effects and cost.

Numerical modelling is the effective alternative approach adopted by numerous researchers. Without considering the wave diffraction and reflection, Li et al. (2011) estimated the wave-induced pore pressure around pile foundation by solving 3D Biot's equation using FEM. Hereafter, a series of investigations by Jeng and his co-workers has been performed to examine dynamic behaviour of the soil in a marine seabed around coastal/offshore structures, such as pipeline (Zhao et al., 2016; Lin et al., 2016), breakwaters (Zhang et al., 2011; Jeng et al., 2013; Ye et al., 2013; Ye et al., 2016), and pile supported structures (Sui et al., 2017, 2019; Zhao et al., 2017). In all these studies, the equations governing the motion of two-phase fluid (RANS and VOF) and the response of seabed were solved by FVM and FEM, respectively. Another monolithically integrated model solving both types of governing equations by using FEM approach was proposed in Lin et al. (2016) to investigate the wave-induced seabed instability (liquefaction potential) in the neighbourhood of partially/fully buried pipeline. Liu et al. (2007) were first to develop a soil solver in OpenFOAM based on the discretised Biot's equation, using FVM for the estimation of wave-induced seabed response surrounding submerged structure. However, this coupled model could not run in a parallel manner as demonstrated in Liu et al. (2007). An extension of poro-elastic model to poro-elasto-plasticity soil model was proposed and implemented in OpenFOAM in Tang (2014), Tang and Hededal (2014), and Tang et al. (2015). In Li et al. (2018) this proposed model was used to investigate the wave-induced momentary liquefaction in the vicinity of gravity-based structure considering the linear elastic structure response of the foundation. For the research on wave-induced seabed response around single/multi-cylinder foundations, Chang and Jeng (2014) performed a numerical investigation of the seabed instability close to a high-rising structure foundation, and concluded that the replacement of surrounding soil layer with a coarse sand layer with greater permeability was a sufficient protection from potential liquefaction. Most recently, by integrating FUNWAVE (Wei et al., 1999; Shi et al., 2001; Kirby et al., 2003) and fully dynamic (FD) form of Biot's equations, Sui et al. (2016) discussed the dynamic soil response caused by small steepness wave. It was concluded that the dynamic behaviour of a porous seabed and a mono-pile were all governed by fully dynamic form of Biot's equations. Lin et al. (2017) proposed a one-way integrated model solving both wave and soil model in OpenFOAM to investigate the nonlinear wave-induced soil response around a large-diameter mono-pile foundation. It was concluded that increasing penetration depth of mono-pile foundation resulted in the decrease of the maximum liquefaction depth around foundation. Recently, the investigation in Zhang et al. (2017) concluded that the existence of upstream piles in an offshore platform may reduce the wave velocity when it approaches downstream piles. Moreover, Tong et al. (2017) suggested that the existence of upstream pile may reduce the wave-induced seabed response near the downstream pile in a twin pile group. Though many studies have been conducted to examine the wave-induced soil response of a porous seabed around various coastal/offshore structures, the soil dynamics in a porous seabed in a multi-cylinder foundation subject to storm wave has not yet been fully understood. A very recent work on the coupled Fluid-Structure-Seabed model has been proposed by Duan et al. (2019), who used IHFOAM and *u-p* approximation for the investigation of the seabed response near mono-pile foundation in combined wave-current environment.

This study focuses on the near-trapping effects on dynamic seabed response and liquefaction close to a multi-cylinder foundation in storm wave condition, which has not been studied yet. The segregated FVM solver proposed in Lin et al. (2017), which incorporates waves2Foam and Biot's equations, is adopted here and further applied to investigate the unknown issue of storm wave-induced soil response around a multi-cylinder foundation. The governing equations for wave and seabed model are described in the Section 2. In Section 3, the simulation of near-trapping phenomenon is validated in detail against available experimental results. Section 4 discusses the distribution of wave pressure, free surface elevation, and liquefaction depth in the vicinity of multi-cylinder structure under two incident wave headings and compares these results with those obtained for a single cylinder. The main conclusions are summarized in Section 5.

2. Numerical model

Two numerical domains are used in the present study, one for incident wave at 0°, as shown in Figure 1, and another one for 45°, as shown in Figure 2. Each numerical domain has two sub-domains, namely a two-phase fluid flow domain (including water and air) and a porous seabed domain. The two-phase fluid flow domain above the seabed is simulated using Waves2Foam (Jacobsen et al., 2012), while the porous seabed behaviour is governed by Quasi-Static (QS) Biot's model. The two sub-models are integrated through the extended General Grid Interpolation (GGI), which incorporates the interpolation of the face and point from zone to zone in terms of non-matched mesh at the interface of flow and seabed sub-domain (Tuković et al., 2014).

2.1 Wave model

The two-phase flow above the seabed surface is simulated by the following mass and momentum equations together with a free-surface tracing function, namely Volume of Fluid (Hirt and Nichols, 1981; Berberović et al., 2009)

$$\nabla \cdot \boldsymbol{u} = 0 \tag{1}$$

$$\frac{\partial \rho \boldsymbol{u}}{\partial t} + \nabla \cdot (\rho \boldsymbol{u})\boldsymbol{u}^{\mathrm{T}} = -\nabla p^{*} - (\mathbf{g} \cdot \boldsymbol{x})\nabla \rho + \nabla \cdot (\mu \nabla \boldsymbol{u}) \tag{2}$$

$$\frac{\partial \alpha}{\partial t} + \nabla \cdot \boldsymbol{u}\alpha + \nabla \cdot \boldsymbol{u}_r \alpha(1-\alpha) = 0 \tag{3}$$

where $\boldsymbol{u}$ is the flow velocity; ρ is the density of fluid; t is the time; $p^{*} = p - \rho \mathbf{g} \cdot \boldsymbol{x}$ is the wave pressure in excess of static pressure; $\mathbf{g}$ is the gravitational acceleration; $\boldsymbol{x}$ is the Cartesian coordinate vector; p is the pressure; μ is dynamic viscosity; $\boldsymbol{u}_r = \boldsymbol{u}_w - \boldsymbol{u}_a$ is the relative flow velocity vector ($\boldsymbol{u}_w$ and $\boldsymbol{u}_a$ are velocity of water and air phase, respectively, Berberović et al., 2009); α is the volume fraction function. $\alpha = 1$ indicates the computational cell is occupied by water, while $\alpha = 0$ denotes that a cell is full of air, and the cell with water-air mixture has $0 < \alpha < 1$. The momentary fluid density and dynamic viscosity are obtained from following equations:

$$\rho = \alpha\rho_w + \rho_a(1-\alpha) \tag{4}$$
$$\mu = \alpha\mu_w + \mu_a(1-\alpha) \tag{5}$$
where the sub-indices *w* and a correspond to water and air, respectively.

At the seabed, mono-pile surface, and lateral boundaries of numerical wave flume, the boundary layer effects are not considered and hence slip boundary is adopted as boundary condition. This is consistent with the study performed by Paulsen et al. (2014b). A pressure outlet condition is specified at the atmospheric boundary on the top of the two-phase flow domain, where air and water can flow out and zero-gradient is applied on the velocity vector fields, but only air can flow in, with a fixed-value condition and water volume fraction being 0 (Chen et al., 2014). For the detailed description of wave generation (inlet boundary) and wave absorption (outlet boundary) zone, the reader is referred to Jacobsen et al. (2012).

2.2 Seabed model

In the hydraulically isotropic porous seabed, the wave-induced dynamic behaviour of soil is governed by QS Biot's equations (Biot, 1941). The mass balance equation adopted in present study is
$$\nabla^2 p_p - \frac{\gamma_w n_s \beta_s}{k_s}\frac{\partial p_p}{\partial t} = \frac{\gamma_w}{k_s}\frac{\partial \varepsilon_s}{\partial t} \tag{6}$$
where p_p is the pore water pressure, γ_w is the unit weight of water, n_s is the porosity of soil, and k_s is the Darcy's permeability. The compressibility of pore fluid β_s and the volumetric strain ε_s are defined, respectively, as:
$$\beta_s = \frac{1}{K_w} + \frac{1-S_r}{P_{w0}} \tag{7}$$
$$\varepsilon_s = \nabla\cdot\boldsymbol{v} = \frac{\partial u_s}{\partial x} + \frac{\partial v_s}{\partial y} + \frac{\partial w_s}{\partial z} \tag{8}$$
where K_w is the true bulk modulus of elasticity of water (taken as 2×10^9 N/m^2, Yamamoto et al., 1978); S_r is the saturation degree of soil; P_{w0} is the absolute pore water pressure; $\boldsymbol{v} = (u_s, v_s, w_s)$ is the vector of soil displacement.

The force equilibrium equation for a poro-elastic seabed can be expressed as:
$$G\nabla^2\boldsymbol{v} + \frac{G}{1-2\nu}\nabla\varepsilon_s = \nabla p_p \tag{9}$$
where G is the shear modulus of soil in relation to Young's modulus (*E*) and Poisson's ratio (ν):
$$G = \frac{E}{2(1+\nu)} \tag{10}$$

The stress-strain relationships for a poro-elastic seabed can be determined on the basis of Hooke's law as
$$\sigma'_x = 2G\left(\frac{\partial u_s}{\partial x} + \frac{\nu}{1-2\nu}\varepsilon_s\right),\ \sigma'_y = 2G\left(\frac{\partial v_s}{\partial y} + \frac{\nu}{1-2\nu}\varepsilon_s\right) \tag{11}$$

$$\sigma_z' = 2G\left(\frac{\partial w_s}{\partial z} + \frac{v}{1-2v}\varepsilon_s\right), \tau_{xy} = \tau_{yx} = G\left(\frac{\partial u_s}{\partial y} + \frac{\partial v_s}{\partial x}\right) \tag{12}$$

$$\tau_{xz} = \tau_{zx} = G\left(\frac{\partial u_s}{\partial z} + \frac{\partial w_s}{\partial x}\right), \tau_{yz} = \tau_{zy} = G\left(\frac{\partial v_s}{\partial z} + \frac{\partial w_s}{\partial y}\right) \tag{13}$$

where σ_i' is effective normal stress, τ_{ij} is shear stress, the subscripts $i,j=x,y,z$ denote the directions of Cartesian coordinates.

To solve QS Biot's equations, the following boundary conditions are prescribed at the boundaries of porous seabed domain and cylinder surface. The upper boundary of seabed domain, namely seabed surface (y=0 in Figure 2 and Figure 3), is the pressure boundary with the pore water pressure, p_p, equal wave pressure, p^*. Furthermore, the vertical shear stresses and effective normal stress are set as 0 at the seabed surface:

$$\sigma_y' = \tau_{xy} = \tau_{yz} = 0,\ p_p = p^* \text{ at } y = 0 \tag{14}$$

The bottom of seabed (y = -h_s, where h_s is the soil depth, Figure 2 and Figure 3) is selected as an impermeable rigid boundary, where no vertical flow and no soil displacement occur:

$$u_s = v_s = w_s = \frac{\partial p_p}{\partial y} = 0 \text{ at } y = -h_s \tag{15}$$

The lateral boundaries of seabed domain are set as impermeable rigid boundaries (Chang and Jeng, 2014):

$$u_s = v_s = w_s = 0, \frac{\partial p_p}{\partial x} = 0 \text{ at } x = 0 \text{ and } x = L_s \tag{16}$$

$$u_s = v_s = w_s = 0,\ \frac{\partial p_p}{\partial z} = 0 \text{ at } z = -W_s/2 \text{ and } z = W_s/2 \tag{17}$$

The sizes of both flow and seabed domain are designed with sufficient length (L_s) and width (W_s) to eliminate the effect from lateral boundaries. Ye and Jeng (2012) suggested that the length of seabed domain should be more than double wavelength to avoid the effect of lateral boundaries on the simulation results within zone of interest, so L_s and W_s are taken as 4.5 times the wavelength (L_w) and 16 times the diameter of cylinder (D). The centres of two different layouts of four cylinders in Figure 2 and Figure 3 and the centres of both flow and seabed domains coincide, so the simulation results around cylinders are not affected by the lateral boundary conditions. In addition, the cylinders are assumed to be rigid impermeable objects and their surfaces are treated as no-flow boundary conditions with zero pore water pressure gradient:

$$\frac{\partial p_p}{\partial \boldsymbol{n}} = 0 \tag{18}$$

where $\boldsymbol{n}$ is the direction normal to the surface of a cylinder. No-flow boundary condition is generally adopted for the surface of rigid object buried/penetrated into a porous seabed (Chang and Jeng, 2014; Lin et al., 2016). Therefore, the interaction between soil and cylinder foundation, which is caused by the fluid-induced cylinder vibration, is not considered here. For the related works considering two-way coupled soil-structure interactions, readers are referred to Tong et al. (2019).

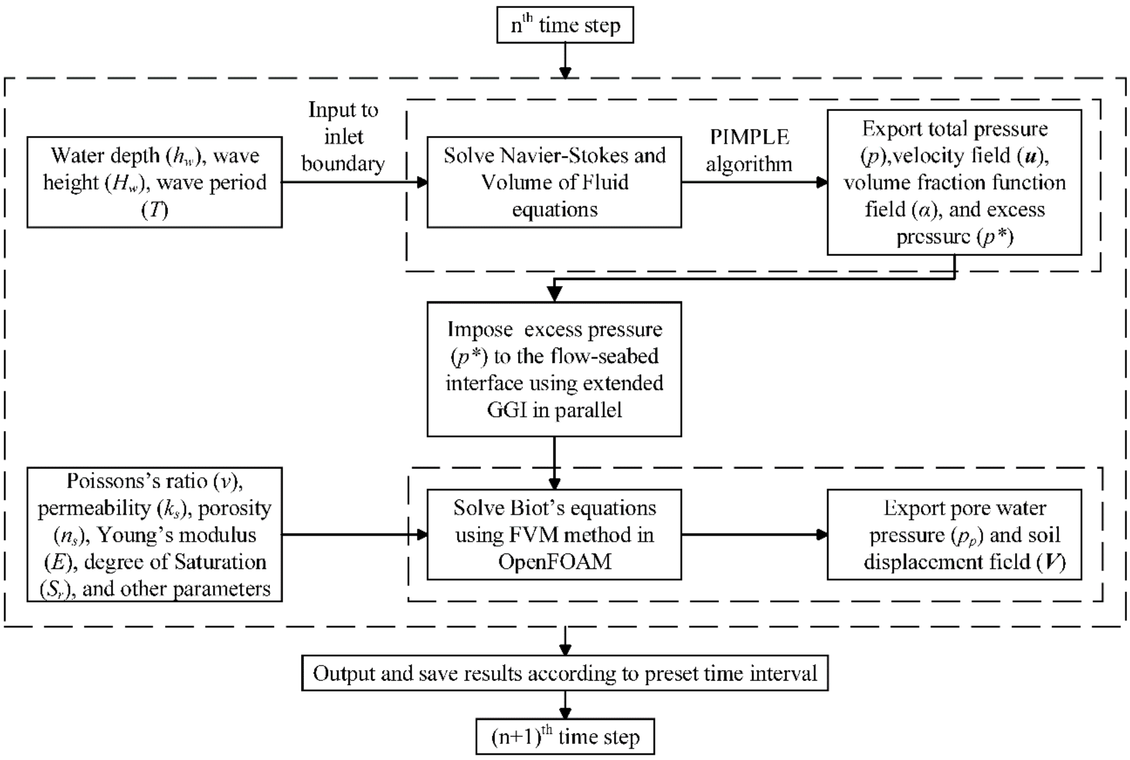

Figure 1 Integrated process of WSSI model

2.3 Integrated process between wave and seabed model

The aforementioned sub-models are integrated through one-way process, as shown in Figure 1. Within one time step the integrated model solves the wave and seabed models individually: the dynamic wave pressure (p*) at the flow-seabed interface calculated by the wave model (waves2Foam) is imposed as the boundary condition to the seabed model by using extended general grid interpolation (GGI) in parallel (Tuković et al., 2014). The detailed interpretation of integration process can be found in Lin et al. (2017). In the present study, the adjustable time step for both flow and seabed model is determined by Courant-Friedrichs-Lewy (CFL) condition with the value of 0.5.

Table 1 Wave and cylinder parameters for validation

Experiments	Case	Wave amplitude, A (m)	Wave period, T (s)	Water depth, h_w (m)	Cylinder diameter, D (m)	$k_w r$	$k_w A$
Ohl et al. (2001b)	1	0.0925	1.25	2	0.406	0.524	0.238
	2	0.049					0.126
	3	0.0589	1.326	2	0.406	0.465	0.135

Note: k_w is wave number; r is cylinder radius.

3. Validation

The wave and soil components of the present integrated model have been validated for a mono-pile in Lin et al. (2017). In this section, the cases with an array of four cylinders are validated against the available experimental data for the two layouts shown in Figure 2 and Figure 3 with 0° and 45°

incident waves, respectively. The parameters for validation are listed in Table 1, where A is wave amplitude, T is wave period, D is cylinder diameter, k_w is wave number, and r is cylinder radius. For the validation of the soil model, readers are referred to Lin et al. (2017). Hence in this section, only the capability of the wave model to simulate the free surface elevation due to wave interaction with four cylinders is investigated.

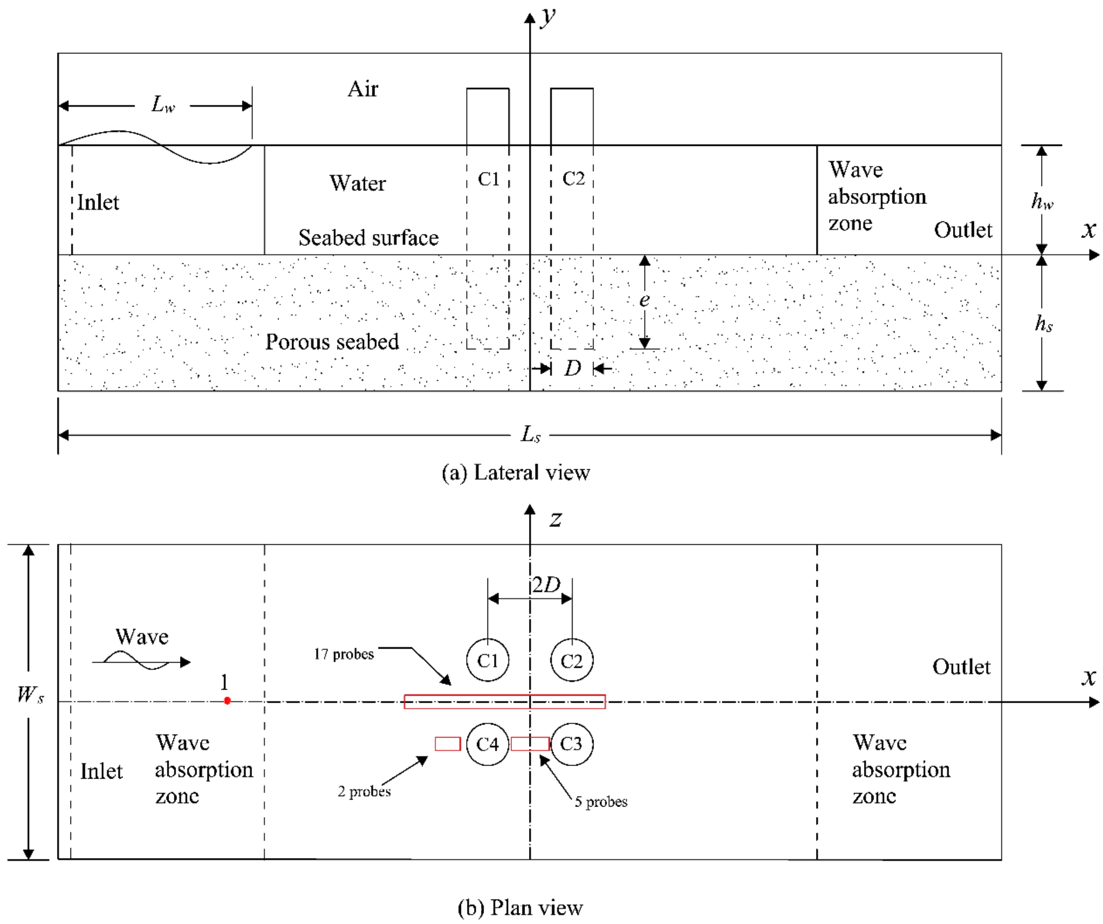

Figure 2 Sketch of the numerical wave tank with 0° incident wave. (a) Lateral view, (b) Plan view; the red dot 1 in plan view is the wave probe for measuring incident wave; the red rectangular zones are locations of other wave probes.

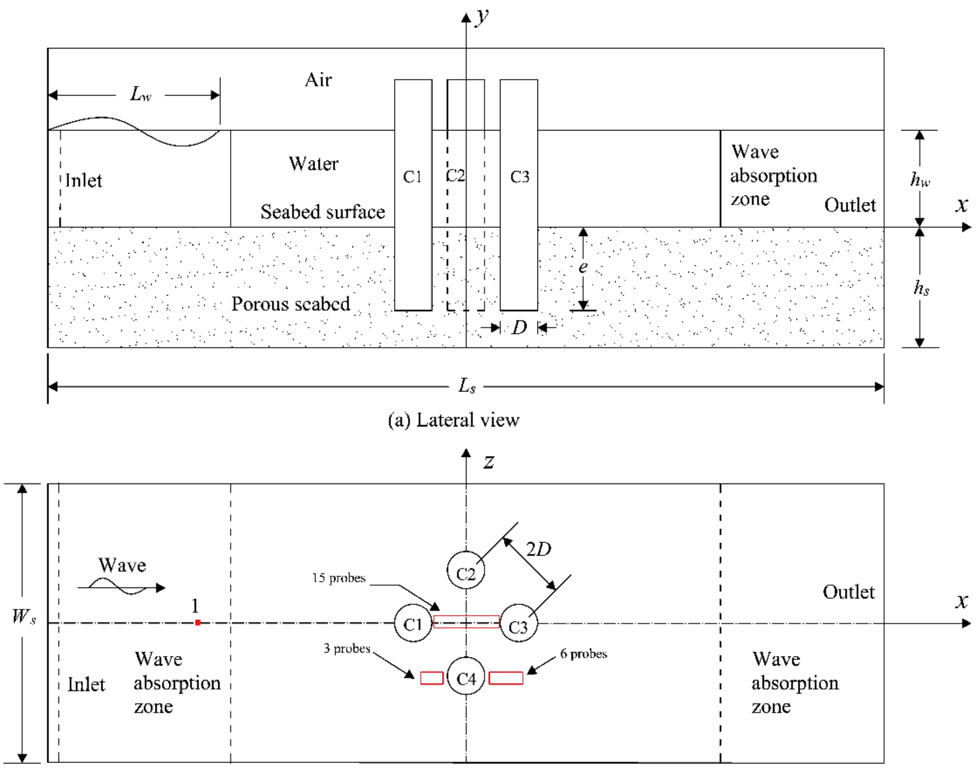

(a) Lateral view

(b) Plan view

Figure 3 Sketch of the numerical wave tank with 45° incident wave. (a) Lateral view, (b) Plan view; the red dot 1 in plan view is the wave probe for measuring the incident wave; the red rectangular zones are locations of other wave probes.

The wave with two incident angles (0° and 45°) is considered. The experimental results performed in Ohl et al. (2001a) are used to validate free surface elevation surrounding an array of closely placed cylinders, where the space between the centres of two neighbouring cylinders is 2*D*. The overall configurations of 3-D numerical domains are the same as those in Figure 2 and Figure 3, except that the soil subdomain is excluded, because it was not present in the experiments. The locations of wave probes are listed in Table 2. Near-trapping phenomenon is investigated for several different types of regular waves, including high and low steepness wave (see Table 1). The still water level and the diameter of the individual cylinders are 2m and 0.406m, respectively. In accordance with the studies of mesh sensitivity conducted in Paulsen et al. (2014b), the mesh for flow domain is refined to at least a resolution of 15 points per wave height for validations and further applications.

The first validation of wave model is carried out with Case 3 (A = 0.0589 m, T = 1.325 s) and the comparisons between simulated and experimental results are presented in Figure 4 for two incident regular waves (0° and 45°). It can be seen in Figure 4(a) that the free surface elevation (η) of the incident wave is in a fairly good agreement with the experimental result in an empty wave tank without any cylinders. For experiments/simulations with an array of cylinders the comparison in Figure 4(b) shows the simulated free surface elevation with 0° heading wave at wave probe A9 agrees well with the experimental data, except for the slight discrepancy of the amount of water merging after each wave crest and before the wave trough. It can be seen in Figure 5 that the small jump between wave crest and trough is caused by the small amount of water propagating from downstream to upstream. This small amount of water continues to propagate from the centre of the array to wave gauge A9, and merges with incoming wave trough, leading to the smaller free surface elevation at wave gauge A9. In Figure 4(c), the same experimental data at wave probe A9 are compared with the simulated results at the centre of array (x=0, z=0), which is only 0.05m away from A9, measured along the central line in the upstream direction. Figure 4(c) demonstrates that a slight shifting of the observation point yields a better agreement at the aforementioned discrepancy.

Table 2 Wave probe locations in Figure 2 and Figure 3

Probe (0°)	x (m)	z (m)	Probe (45°)	x (m)	z (m)
1	-4.5	0	1	-4.5	0
B10	-1.15	0	D9	-0.35	0
B9	-1.05	0	E6	-0.3	0
B8	-0.95	0	D8	-0.25	0
B7	-0.85	0	E5	-0.2	0
B6	-0.75	0	D7	-0.15	0
B5	-0.65	0	E4	-0.1	0
B4	-0.55	0	D6	-0.05	0
B3	-0.45	0	D5	0	0
A12	-0.35	0	D4	0.05	0
A11	-0.25	0	E3	0.1	0
A10	-0.15	0	D3	0.15	0
A9	-0.05	0	E2	0.2	0
A8	0.05	0	D2	0.25	0
A7	0.15	0	E1	0.3	0
A6	0.25	0	D1	0.35	0
A5	0.35	0	D12	-0.325	-0.575
A4	0.45	0	D11	-0.275	-0.575
B12	-0.765	-0.407	D10	-0.225	-0.575
B11	-0.665	-0.407	E12	0.22	-0.575
B2	-0.15	-0.407	E11	0.32	-0.575
B1	-0.05	-0.407	E10	0.37	-0.575
A3	0.05	-0.407	E9	0.42	-0.575
A2	0.1	-0.407	E8	0.47	-0.575
A1	0.15	-0.407	E7	0.52	-0.575

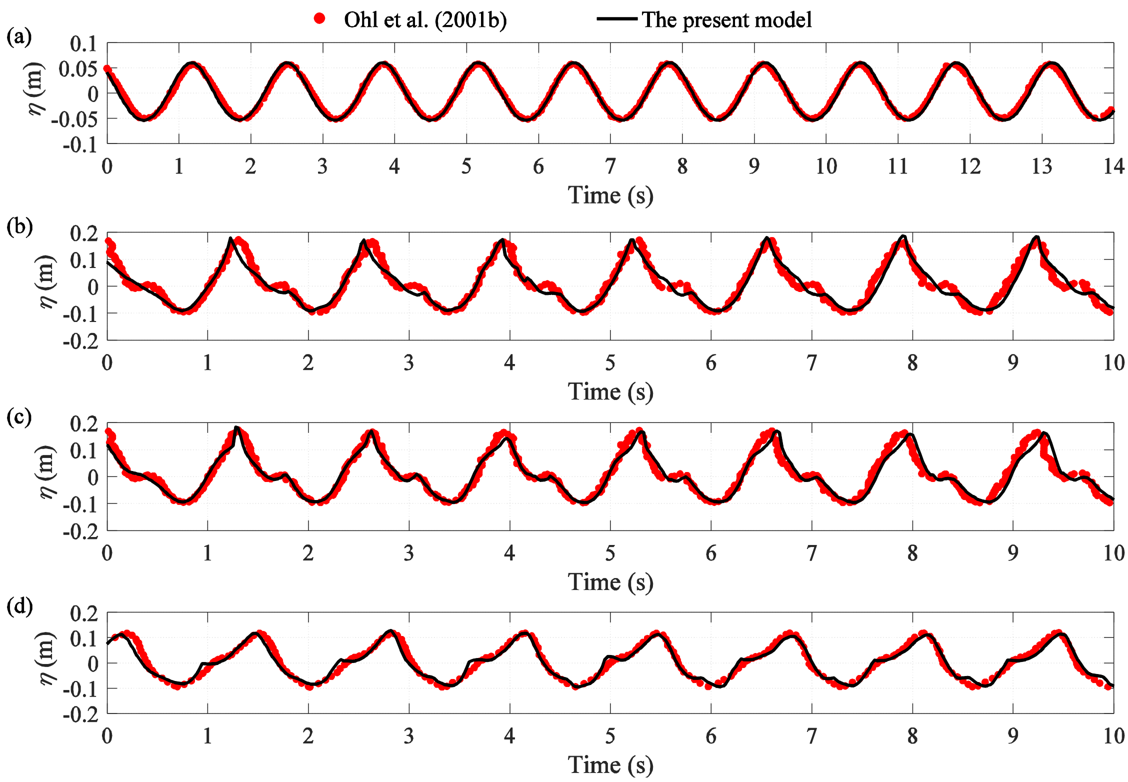

Figure 4 Time history of free surface elevation (η) of simulated and experimental results (Case 3 in Table 1). (a) Wave probe 1; (b) Wave probe A9 with 0° heading; (c) Centre of an array (x=0 and z=0) with 0° heading; (d) Wave probe E2, with 45° heading.

For a 45° heading wave with same parameters as 0° heading, the simulated and experimental results are compared in Figure 4(d), where a generally good agreement is demonstrated, with just a minor discrepancy before the arrival of individual wave crest. Comparison of the magnitude of both simulated and experimental results in Figure 4(b-d) with those for incident wave in Figure 4(a) shows that significant amplifications of the magnitude of both wave crest and wave trough resulted from wave-cylinders interaction. This amplification process of free surface elevation is termed near-trapping phenomenon. On the basis of above validations, it can be concluded that the developments of free surface elevation at typical locations within an array of cylinders are well predicted by numerical simulations.

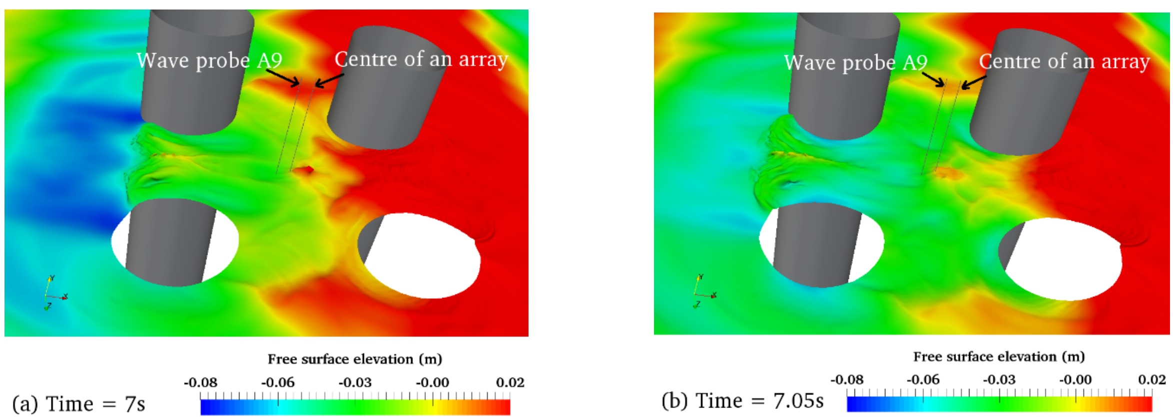

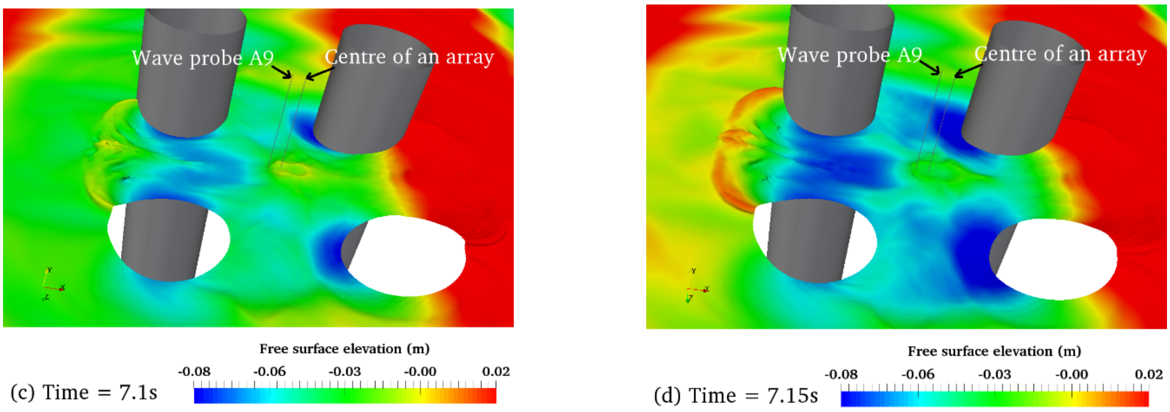

Figure 5 Snapshots of free surface elevation (η) at different moments for Case 3 in Table 1. (a) Time = 7s; (b) Time = 7.05s; (c) Time = 7.1s; (d) Time = 7.15s.

Further validations of wave model results for free surface elevation in the vicinity of cylinders are performed in frequency domain. For this purpose the time history of simulated results at various locations of wave probes indicated in Figure 2 and Figure 3 are processed by Fast Fourier Transforms (FFTs). The same processing procedure and approach used in Ohl et al. (2001a) are adopted here to extract the spectral peaks at single ($f = f_i$, f_i is incident wave frequency), double ($f = 2f_i$), triple ($f = 3f_i$) incident wave frequencies, and all spectral components within the range of ($f \pm 0.25 f_i$). These separated frequency components are termed first-, second-, and third-order harmonics, respectively. After that, each separated spectral component is further processed by Inverse FFTs (IFFTs) to obtain the corresponding time series, from which mean values of all the peaks are computed and compared with those for data measured at various locations of wave probes.

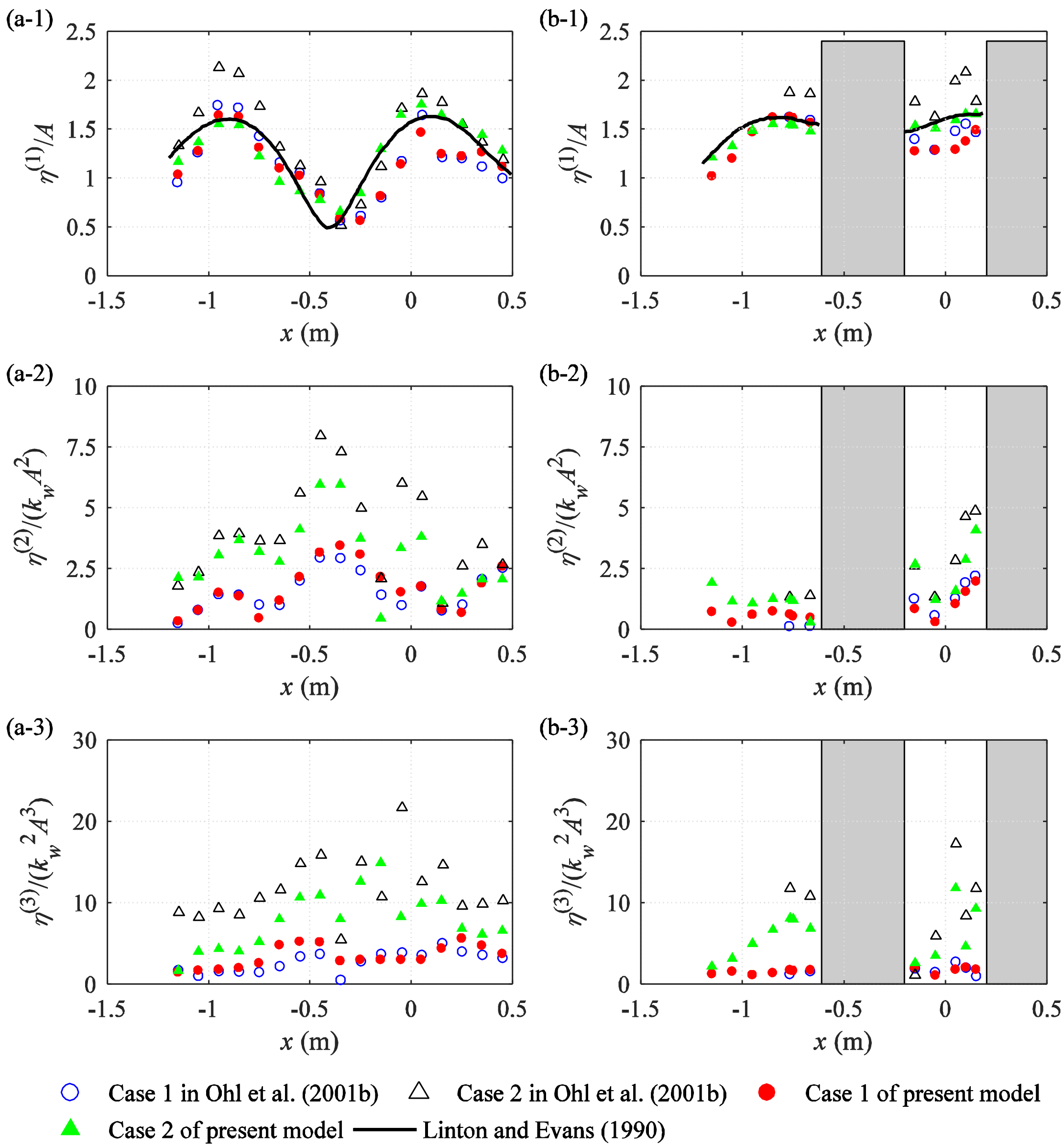

Figure 6 Comparison between simulated and experimental results of Case 1 and Case 2 with 0° heading. (1) First-order harmonics; (2) Second-order harmonics; (3) Third-order harmonics. (a) and (b) indicate the probes at central and lateral sides, respectively. Keys for symbols:

337

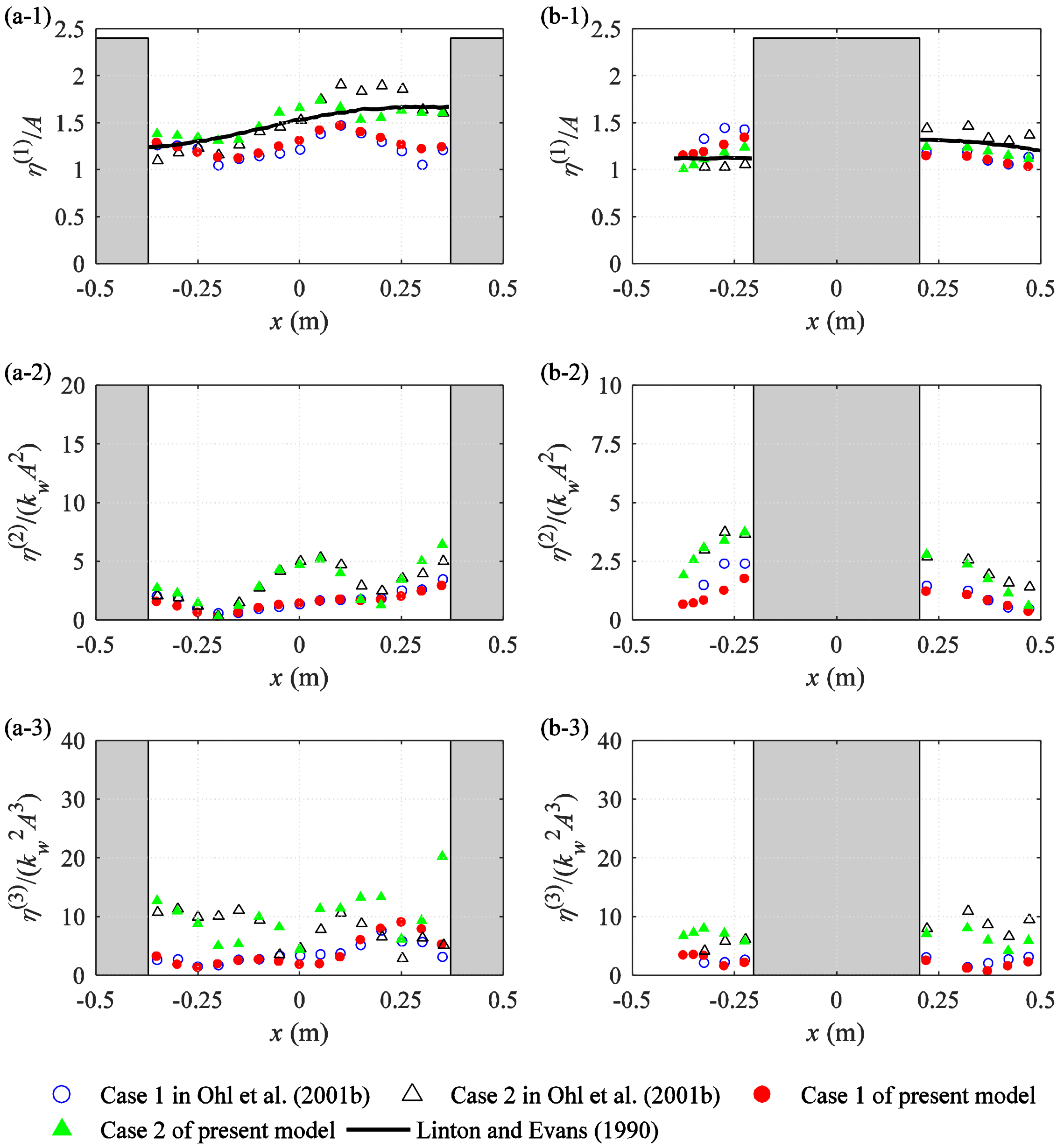

Figure 7 Comparison between simulated and experimental results for Case 1 and Case 2 with 45° heading. (1) First-order harmonics; (2) Second-order harmonics; (3) Third-order harmonics. Columns (a) and (b) indicate the probes at central and lateral sides, respectively. Keys for symbols: (do the same as for figure 6)

On the basis of aforementioned post-processing, additional comparisons of different order harmonics at various locations, up to third-order, are presented in Figure 6 for 0° incident angle and in Figure 7 for 45° angle. The wave parameters of each validation case can be found in Table 1. For 0° heading (Figure 6) there are some discrepancies for Case 2 with smaller steepness wave, whereas the agreement for the Case 1 with greater steepness wave is much better. For the incident wave with 45° heading (Figure 7) there is good agreement for both Case 1 and Case 2. In both Figure 6 and Figure 7, the Case 1 with greater steepness wave has a better agreement with experimental results, rather than Case 2 with small wave steepness. From the comparisons of first-order component in Figure 6 and

Figure 7, the evident amplification of free surface elevation, also named near-trapping phenomenon, can be noticed along the central line and at lateral sides of four cylinders. Overall, it can be concluded that the near-trapping phenomenon has been well captured in the present numerical model that can be used to investigate dynamic seabed response around an array of cylinders.

4. Applications

Cylinder foundations supporting offshore wind turbines or platforms are usually protected from the onset of scour. When exposed to harsh ocean environments, scour protections surrounding cylinder foundations are vulnerable to liquefaction. However, the studies concerning liquefaction potential in the vicinity of closely placed cylinder foundations have not been reported yet. The previous investigation in Lin et al. (2017), performed for the wave condition from the Danish 'Wave loads' project (Paulsen et al., 2014b), with KC = 8.85, and k_wD = 0.2, revealed that the maximum wave-induced liquefaction depth in the vicinity of a mono-pile foundation may occur at the lateral sides of the cylinder. In order to study liquefaction in the vicinity of an array of circular cylinders in storm wave conditions and compare it with the results for the single cylinder case, the same wave condition as in Lin et al. (2017) is adopted in the present study. The remaining parameters of incident wave used in present application are given in Table 3, with k_wA being 0.14 in all simulations, and k_wD ranging from 0.2 to 0.43. A constant k_wA value and varying k_wD values were adopted because of the results of Cong et al. (2015), who showed that near-trapping phenomenon is insensitive to k_wA, but highly sensitive to k_wD . The soil parameters used in this study are listed in Table 4. For the studies of varying soil parameters, readers are referred to Chang and Jeng (2014) for details. Individual cylinders are assumed to be rigid objects, and the movement of the cylinder foundations is not simulated. Two layouts of four cylinders investigated in this section are shown in Figure 2 and Figure 3. The location of a point along the perimeter of a cylinder is defined by its angle θ, as shown in Figure 8.

Table 3 Wave properties for the investigation of wave-cylinders-seabed interaction

Case	Wave amplitude, A (m)	Wave period, T (s)	Wave length, L_w (m)	k_wD	Water depth, h_w (m)
1	2.43	9.2	108.45	0.35	
2	2.88	10.5	129.12	0.29	
3	3.425	12.05	153.12	0.25	20
4	4.215	13.6	188.5	0.2	
5	1.94	7.88	86.79	0.43	

Table 4 Parameters for seabed and cylinders

Seabed characteristics			
Seabed thickness, h_s (m)	38	Poisson's ratio, ν	0.4
Young's modulus, E (Pa)	2.8×10^{8}	Permeability, k (m/s)	1×10^{-4}
Degree of saturation, S_r	0.98	Soil porosity, n_s	0.38
Cylinder characteristics			

Diameter, D (m)	6	Penetration depth, e (m)	18
D/L_w	0.032		

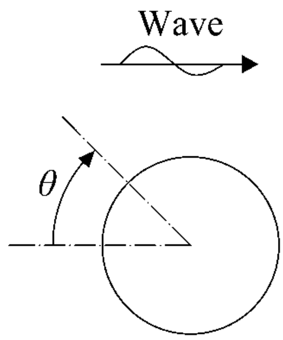

Figure 8 θ-location around a cylinder

4.1 Liquefaction development around cylinders in an array

Momentary liquefaction can take place at a point at a depth L_d (= $-y$) beneath the seabed surface when the difference between the pore pressure at this level, p_p, and the pressure on a seabed surface above the point, P_b, becomes sufficiently large to balance or even exceed the overburden soil weight per unit area. As a result soil matrix becomes incapable of carrying any load and momentary liquefaction occurs. This process contributes to the scour around a cylinder founded in a sand bed (Tonkin et al., 2003). It should be noted that both the p_p, and P_b denote pressure in excess of hydrostatic pressure, so that the overburden soil weight is reduced by the buoyancy force. Due to the assumptions that the cylinder is hollow instead of solid, and the vibration of the cylindrical foundations is not taken into account, the liquefaction criterion is (Jeng, 2013; Sumer, 2014):

$$(\gamma_s - \gamma_w)L_d \le p_p - P_b \tag{19}$$

with γ_s and γ_w denoting seabed and water unit weight, respectively. In present study, $\gamma_s = 1.9\,\gamma_w$ is used to evaluate the weight of the overburden soil.

In this section, the development of liquefaction in the proximity of individual cylinders in an array is analysed for Case 2 with wave period T = 10.5 s (Table 3). The liquefaction depth has been evaluated using criterion (19). Results for each cylinder at the outer surface 0.1m away from the cylinder surface are shown in Figure 9 and Figure 10. In order to show the amplification of liquefaction induced by near-trapping phenomenon, the liquefaction depth (L_d) near a four-cylinder foundation is normalized by the single maximum liquefaction depth ($L_{d\max}^{\mathrm{MP}}$) around a mono-pile foundation in the entire liquefaction zone, i.e. within -17.5m < x < 17.5m and -17.5m < z < 17.5m. The $L_{d\max}^{\mathrm{MP}}$ values of all the single cylinder cases from Table 3 are listed in Table 5. Figure 9(a) and (b) indicate that for 0° wave heading there are two local minima of the liquefaction depth around both C1 and C2 cylinders, occurring at θ equal 0° and 180°, and two local maxima, at θ equal 90° and 270°. Between these local minima and maxima liquefaction depth near the cylinder varies monotonically – it increases from θ=0° to θ=90°, decreases from θ=90° to θ=180°, and then repeats this cycle from θ=

180° to θ=360°. The liquefaction depth at the upstream end of cylinder, at θ=0°, is somewhat smaller for C2, indicating a degree of sheltering by C1.

Table 5: the minimum free surface elevation ($\eta_{\min}^{MP}$), the minimum pore water pressure ($P_{b\min}^{MP}$) on the seabed surface, and the maximum liquefaction depth ($L_{d\max}^{MP}$) around a mono-pile foundation

Case	1	2	3	4
$\eta_{\min}^{MP}$ (m)	-2.84	-3.55	-4.97	-4.32
$P_{b\min}^{MP}$ (Pa)	-1.42×10^4	-1.90×10^4	-2.00×10^4	-2.40×10^4
$L_{d\max}^{MP}$ (m)	1.26	1.8	1.86	2

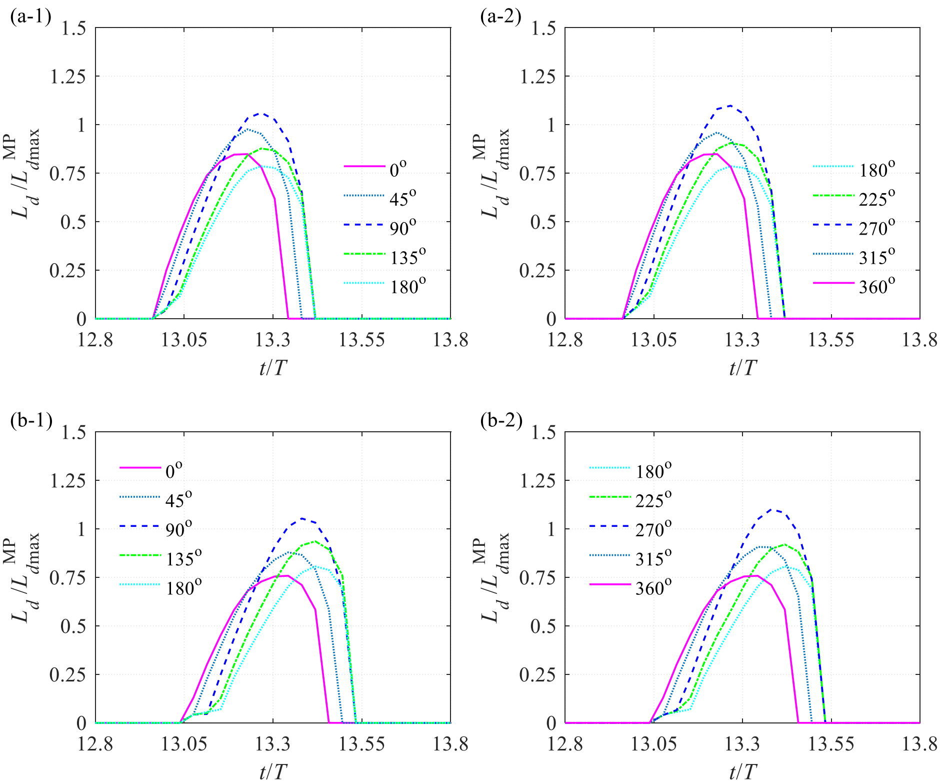

Figure 9 Development of liquefaction depth at various θ-locations with 0° incident wave. (a) C1 cylinder; (b) C2 cylinder. Refer to Figure 8 for the definition of θ, and to Figure 2 for the location of cylinders.

Development of liquefaction depth for 45° incident wave is shown in Figure 10. Owing to the symmetry of liquefaction development along the lateral sides of C1 and C3 cylinders, results are shown only for a half of their perimeter, from θ=0° to θ=180°, in Figure 10(a) and (b), respectively.

For the same reason results are presented along the entire perimeter for C2, but not for C4, where they are identical. The overall development of liquefaction depth around the perimeter of each individual cylinder is similar to that already seen for 0° heading wave. However, there is a notable difference between the values of the local minima of liquefaction depth at θ=0° for cylinders C1 and C3 – the former is much deeper than the latter, leading to the conclusion that the upstream end of C3 is protected by the three upstream cylinders. Comparison of the liquefaction development for groups of cylinders (Figure 9 and 10) with that for mono-pile (Figure 11) shows that the maximum momentary liquefaction depth in all cases takes place at θ=90° and the magnitudes of liquefaction depth at all locations in both four-cylinder cases have been significantly amplified.

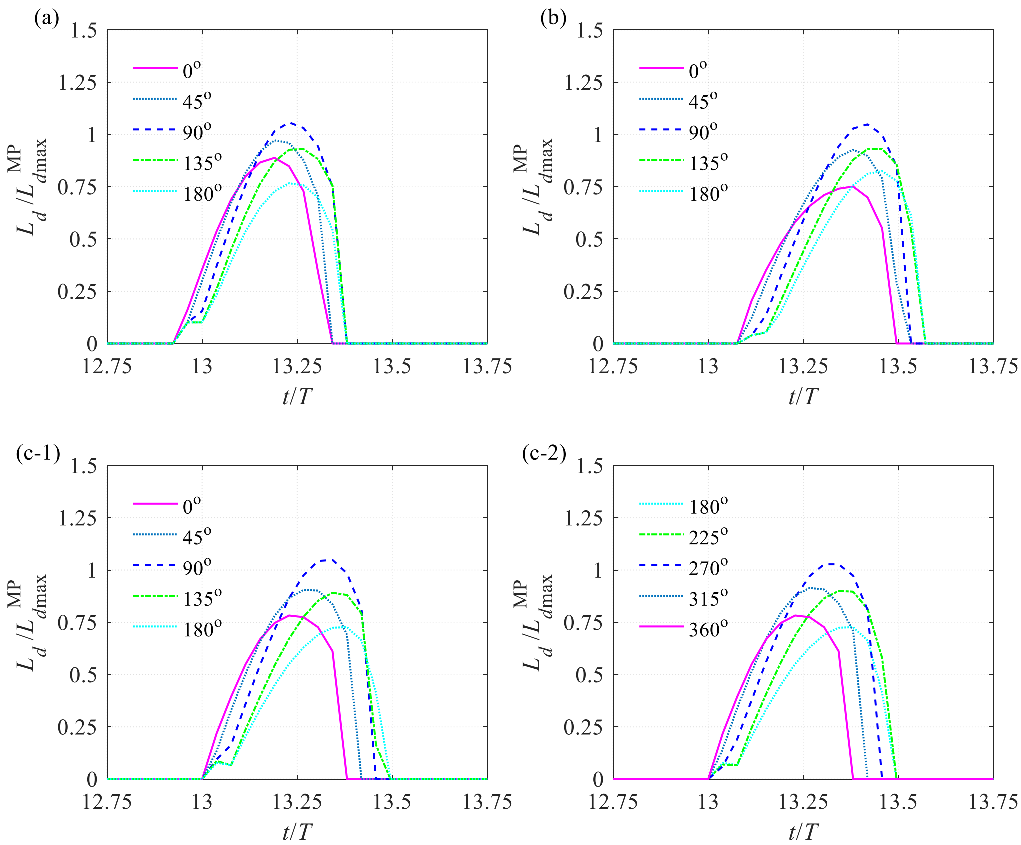

Figure 10 Development of liquefaction depth at various θ-locations with 45° incident wave. (a) C1 cylinder; (b) C3 cylinder; (c) C2 cylinder. Refer to Figure 8 for the definition of θ, and to Figure 3 for the location of cylinders.

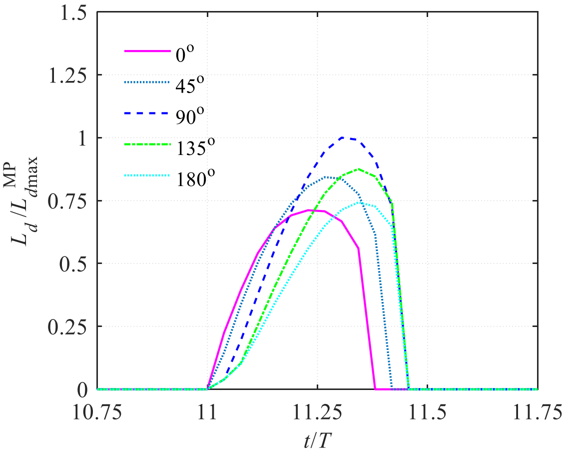

Figure 11 Development of liquefaction depth at various θ-locations with a mono-pile foundation. Refer to Figure 8 for the definition of θ.

4.2 Vertical distribution of pore water pressure around cylinders

For momentary liquefaction, the primary cause is attributed to the difference between the pore water pressure at seabed surface and a position beneath. As shown in section 4.1, the development of liquefaction depth around each cylinder in a cylinder array has been amplified by the near-trapping phenomenon of incident wave, which reduces the minimum free surface elevation during wave passage, and decreases the minimum wave-induced pressure at the seabed, resulting in deeper momentary liquefaction. In this section, in order to better understand the distribution of the maximum liquefaction depth around the perimeter of each cylinder, the liquefaction depth is estimated along an outer surface 0.1m away from cylinder surface at the moment when liquefaction depth reaches its maximum, such as t/T= 13.3 in Figure 9(a), and compared with those of a mono-pile foundation. Liquefaction depths are shown in Figures 12, 13, and 14 on the top of the contour plot of pore water pressure recorded at the same moment (p_p), normalized with the minimum pore water pressure ($P_{b\min}^{MP}$, listed in Table 5) on the seabed surface in a mono-pile foundation case. The distribution of the liquefaction depth around the mono-pile perimeter is in qualitative agreement with experimental results of Tonkin et al. (2003), who also found the deepest scour at the cylinder side (θ=90°), albeit for tsunami waves rather than non-linear periodic waves used in the present study.

Figure 12 for 0° wave heading shows that the distributions of both pore water pressure and liquefaction depth around C1 and C2 cylinders are non-symmetric, unlike distributions along a mono-pile case foundation in Figure 13, which are symmetric with respect to θ=180°. A slightly non-symmetric distribution of liquefaction depth and pore water pressure near C2 cylinder is also indicated for 45° wave heading, in Figure 13(b), while these distributions near C1 and C3 cylinders are symmetric. For both 0° and 45° incident wave cases the inner zone (180°<θ<360°) towards the centre of the cylinder array shows more significant liquefaction than that of the outer zone (0°<θ<180°), away from the cylinder array centre. Moreover, the overall liquefaction depth and pore water pressure on seabed surface in the vicinity of each cylinder in a cylinder array are greater than those around a mono-pile foundation. As stated earlier, this can be explained by the near-trapping phenomenon induced by wave-cylinders interaction above the seabed.

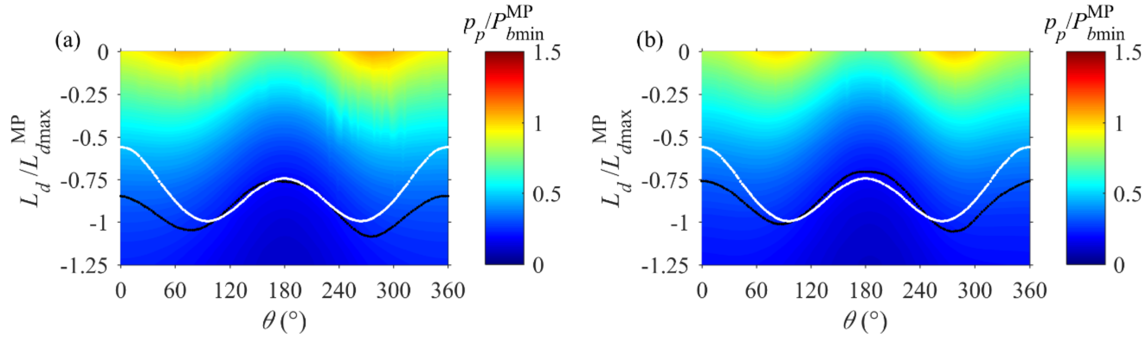

Figure 12 Pore water pressure and liquefaction depth for 0° incident wave along an outer surface at 0.1m distance from cylinder at the moment when the maximum liquefaction depth occurs. (a) C1 cylinder at t/T= 13.3; (b) C2 cylinder at t/T=13.4. Black line shows liquefaction depth around individual cylinders in a cylinder array and white line shows liquefaction depth around mono-pile foundation. Refer to Figure 8 for the definition of θ, and to Figure 2 for the location of cylinders.

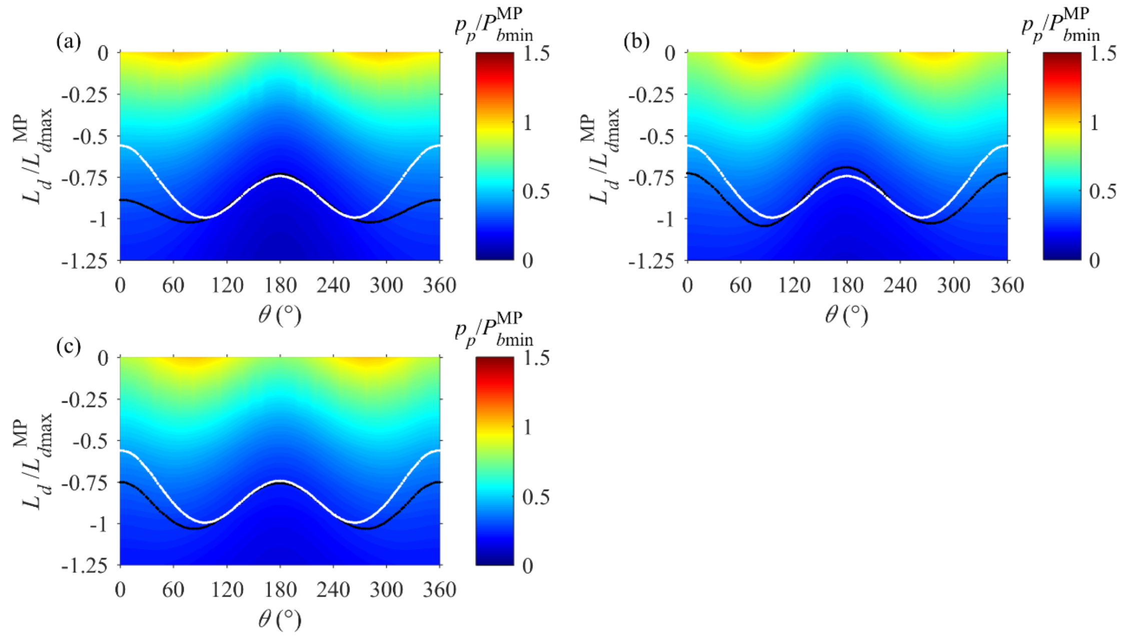

Figure 13 Pore water pressure and liquefaction depth for 45° incident wave along an outer surface at 0.1m distance from cylinder at the moment when the maximum liquefaction depth occurs. (a) C1 cylinder at t/T= 13.3; (b) C2 cylinder at t/T=13.37; (c) C3 cylinder at t/T=13.45. Black line shows liquefaction depth around individual cylinders in a cylinder array and white line shows liquefaction depth around mono-pile foundation. Refer to Figure 8 for the definition of θ, and to Figure 3 for the location of cylinders.

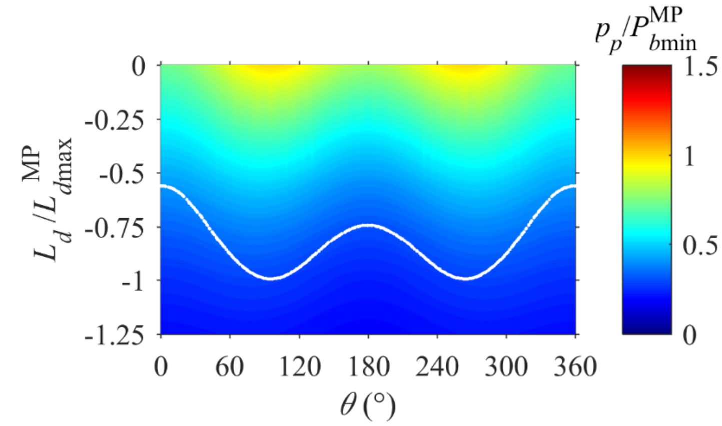

Figure 14 Pore water pressure and liquefaction depth along an outer surface at 0.1m distance from mono-pile foundation at the moment t/T=11.35 when the maximum liquefaction depth occurs. White line shows liquefaction depth around mono-pile foundation. Refer to Figure 8 for the definition of θ.

4.3 Spatial distribution of the maximum values of liquefaction, pore water pressure on seabed surface, and free surface elevation

This section investigates the spatial distribution of the wave-induced liquefaction around individual cylinders in an array. Figure 15 shows the spatial distribution (in *x*-*z* plane) of the maximum liquefaction depth (L_d) within a wave period (calculated from stable results after 8 wave periods) for Case 1 to Case 4. As before the maximum liquefaction depth is normalized with the maximum liquefaction depth ($L_{d\max}^{\mathrm{MP}}$) of a mono-pile foundation with the identical incoming wave. The analogous post-processing is also applied to the minimum water pressure on the seabed surface (P_{bmin}) and the minimum free surface elevation (η_{min}), and the associated results are shown in Figure 16 and Figure 17, respectively. Since liquefaction depth in the Case 5 with a mono-pile foundation is small, the discussion of this case will be presented later, in section 4.5.

Comparison of the normalized maximum liquefaction depths for 0° and 45° incident waves with those for a mono-pile foundation case (Figure 15) shows that the amplification factors for the maximum liquefaction depth range approximately from 1.05 to 1.2. Moreover, under the action of 0° incident wave amplification of liquefaction depth is more noticeable (Figure 15a), then for 45° incident wave (Figure 15b), especially at the lateral sides of front cylinders (C1 and C4 for 0° incident wave, and C1 for 45° incident wave). The maximum momentary liquefaction zones are located at the lateral sides of individual cylinders, and between the two front cylinders (C1 and C4) for 0° incident wave. This agrees with Cong et al. (2015) who concluded that the amount of incoming wave is trapped in the zone between C1 and C4 and the inner zone of a four-cylinder structure is shielded without significant amplification. At the lateral sides of cylinders in Figure 15(a), the decrease of k_wD from 0.35 (shorter wave) to 0.25 (longer wave) leads to the more significant amplification on liquefaction depth, but for k_wD of 0.2 (Case 4) the amplification factor reduces to approximately 1.05. A possible explanation is that due to the greater wave length in Case 4 the four-cylinder group behaves as a unity. The distribution of liquefaction around a cylinder group is therefore similar to that around a mono-pile foundation, where the smaller liquefaction depth is also shown in front of the cylinder array.

Figure 16 shows the spatial distribution of the minimum wave-induced pressure on seabed surface, P_b. It is very similar to the distribution of the maximum liquefaction depth shown in Figure 15, indicating that reduction of P_b is the primary cause of the momentary liquefaction. The minimum seabed pressure P_b is in turn associated with the minimum free surface elevation, shown in Figure 17. However, although their general distribution is similar, free surface elevation seems to be more violent and contains higher-order harmonic components (Readers are referred to the Fig.8 and Fig.9 in Lin et al. (2017) for the temporal comparisons of these three variables). This is because wave pressure attenuation with water depth is frequency dependent, so the attenuation of wave pressure for higher harmonic components is faster than that for lower frequency harmonics, hence higher order harmonic components attenuate between the water surface and the seabed surface and do not reach the latter. Consequently the near-trapping phenomenon of wave-induced pressure on seabed surface and the resulting momentary liquefaction are somewhat different from that of free surface elevation, which contains higher-order harmonic components. The spatial distribution of the minimum free surface elevation ($\eta_{\min}$) in Figure 17 further confirms that the incident wave though trapped inside the cylinder array causes lower water levels within the inner zone compared with those outside.

To demonstrate the overall effect of the near-trapping on a cylinder group, and compare it with a mono-pile, the amplification factors averaged over the previously defined liquefaction zone (-17.5m $< x <$ 17.5m and -17.5m $< z <$ 17.5m) are shown in Figure 18, together with the minimum and the maximum amplification factors. It can be seen that the average amplification factor does not linearly increase with the decrease of k_wD and the increase of wave period. The sudden increase of amplification factor at k_wD = 0.25 (T = 12.05s) is also confirmed by both experimental results and numerical simulation in Cong et al. (2015) for investigating the effect of near-trapping phenomenon, but the overall development of amplification factors tends to stabilize with the increase of wave period. It can be noticed that the developments of amplification factor with k_wD for liquefaction depth, wave pressure on seabed surface, and free surface elevation, follow similar patterns. Moreover, the amplification factors for liquefaction depth and wave pressure on seabed surface are similar, while the effect of the near-trapping phenomenon on free surface elevation is more pronounced. The incident wave for two different incident angles are found to be trapped in a four cylinder structure, and result in the noticeable amplification factor compared to that of a mono-pile case. For the incoming wave angles, it can be seen that the incident wave with 0° heading seems to be trapped easier than that of 45° headings and mono-pile case, leading to greater amplification factors.

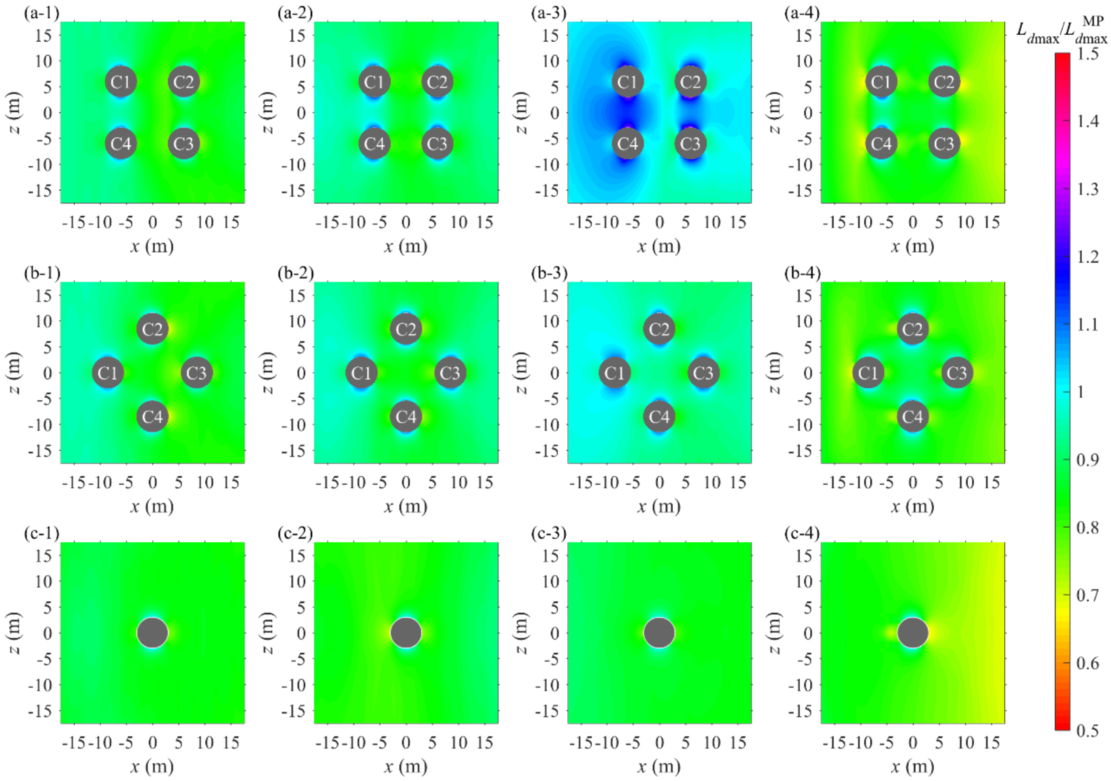

Figure 15 Spatial distribution of the normalized maximum liquefaction depth ($L_{d\max}$) within a wave period over the maximum liquefaction depth ($L_{d\max}^{MP}$) in the mono-pile case with same incident wave. (a) 0° incident wave; (b) 45° incident wave; (c) a mono-pile case. The numbering indicates the case number in Table 3.

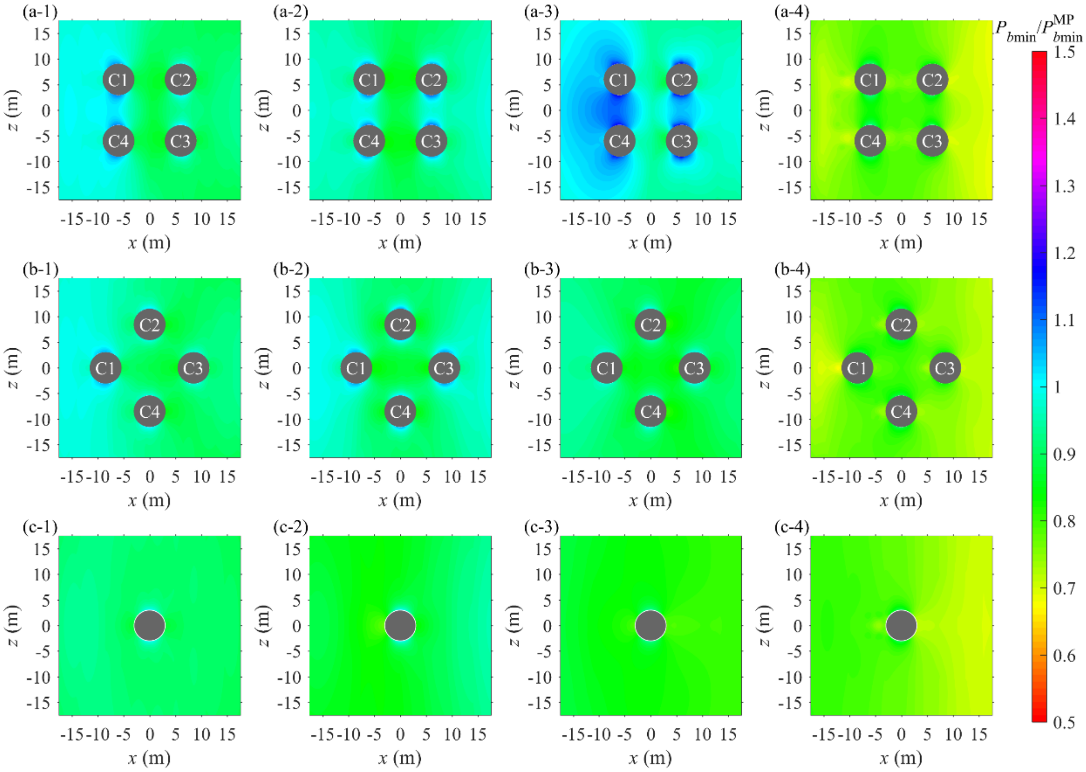

Figure 16 Spatial distribution of the normalized minimum pore water pressure at seabed ($P_{b\min}$) within a wave period over the minimum pore water pressure ($P_{b\min}^{\mathrm{MP}}$) in the mono-pile case with same incident wave. (a) 0° incident wave; (b) 45° incident wave; (c) a mono-pile case. The numbering indicates the case number in Table 3.

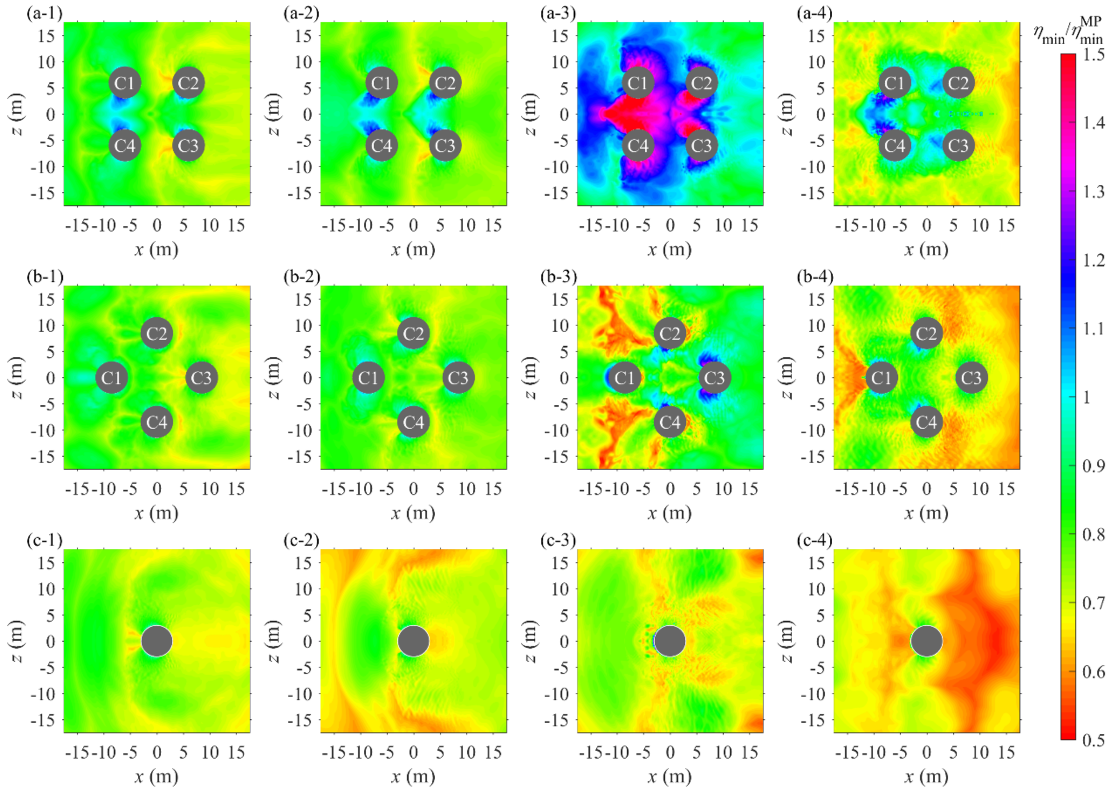

Figure 17 Spatial distribution of the normalized minimum free surface elevation ($\eta_{\min}$) within a wave period over the minimum free surface elevation ($\eta_{\min}^{MP}$) in the mono-pile case with same incident wave. (a) 0° incident wave; (b) 45° incident wave; (c) a mono-pile case. The numbering indicates the case number in Table 3.

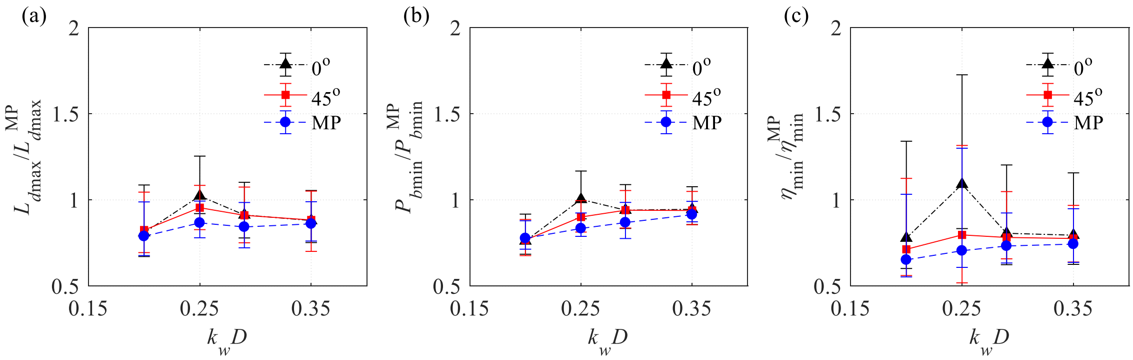

Figure 18 Average, the minimum, and the maximum amplification factors for different layouts and k_wD; (a) liquefaction depth L_d; (b) seabed surface pressure P_b; (c) free surface elevation η.

4.4 Influence of incident angle

For a better understanding of how the maximum liquefaction depth is distributed around each cylinder surface, the maximum liquefaction across the same vertical circular plane as in Figure 9 and Figure 10 for two incident wave angles are compared with the result of a single cylinder case (Figure 11) and presented in Figure 19. Good protection effect of the upstream cylinder (C1) on the vicinity of the front (0°) and back (180°) of downstream cylinder (C2 with 0° wave heading and C3 with 45°

wave heading) can be confirmed in all cases with both incident angles. A special attention needs to be paid to the back side of each downstream cylinder, where the maximum momentary liquefaction depth is smaller than that at the back side of upstream cylinder. This can also be attributed to the protection effect from front cylinders. Comparing the liquefaction depth around individual cylinders in an array with the result of a mono-pile foundation case, it is evident that the liquefaction depth with a four-cylinder foundation is overall greater, and the upstream cylinder(s) experience more significant liquefaction threat than other cylinders in an array.

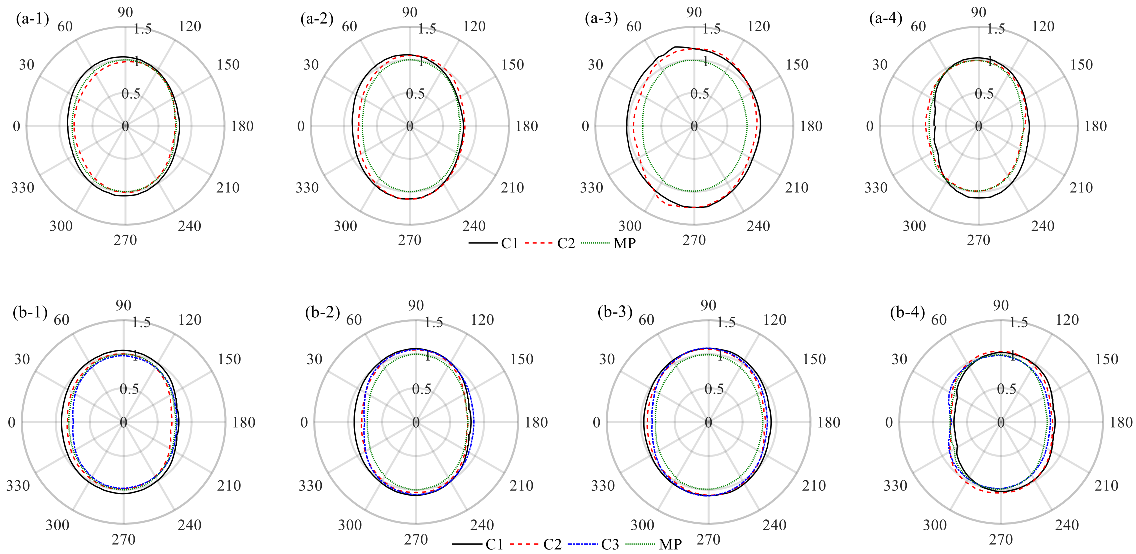

Figure 19 Polar plot of the normalized of the maximum liquefaction depth ($L_{d\min}$) within a wave period over the maximum liquefaction depth ($L_{d\max}^{\mathrm{MP}}$) in the mono-pile case with same incident wave. (a) 0° incident wave; (b) 45° incident wave. Refer to Figure 8 for the definition of θ, and to Figure 2 for the location of cylinders. The numbering indicates the case number in Table 3.

On the basis of the spatial distribution of wave-induced pressure on seabed surface in Figure 16, the minimum value is located at the lateral sides of each cylinder. For momentary liquefaction, the primary cause is the wave-induced pressure under wave trough. Therefore, the maximum momentary liquefaction is distributed at both lateral sides of each circular cylinder. Figure 19 further confirms this: the maximum liquefaction depth over a wave period indeed takes place at both lateral sides of each cylinder. Moreover, for 0° incident wave (Figure 19a) the distribution of the maximum liquefaction depth in the vicinity of both upstream and downstream cylinders (C1 and C2) is non-symmetric. In contrast, Figure 19(b) shows that for 45° incident wave the distribution of the maximum liquefaction depth in the vicinity of the lateral cylinder C2 is fairly symmetric.

4.5 Liquefaction around foundation under shorter waves

As aforementioned in section 4.3, the liquefaction depth near a mono-pile foundation in Case 5 (Table 3) is small, so this case is now discussed separately from other four cases. The maximum liquefaction depth over a wave period in Case 5 is presented in Figure 20, where in both incident wave directions liquefaction is most pronounced in front of a cylinder array and liquefaction depth at the back of a cylinder array is smaller. This further confirms the good protection of downstream cylinders by upstream cylinders, which was discussed in sections 4.3 and 4.4: the upstream cylinders (C1 and C4 with 0° wave heading; C1 with 45° wave heading) may encounter more significant liquefaction threat than the downstream cylinders. Regarding the mono-pile foundation, shorter incident wave generates much smaller liquefaction depth in the vicinity of the cylinder.

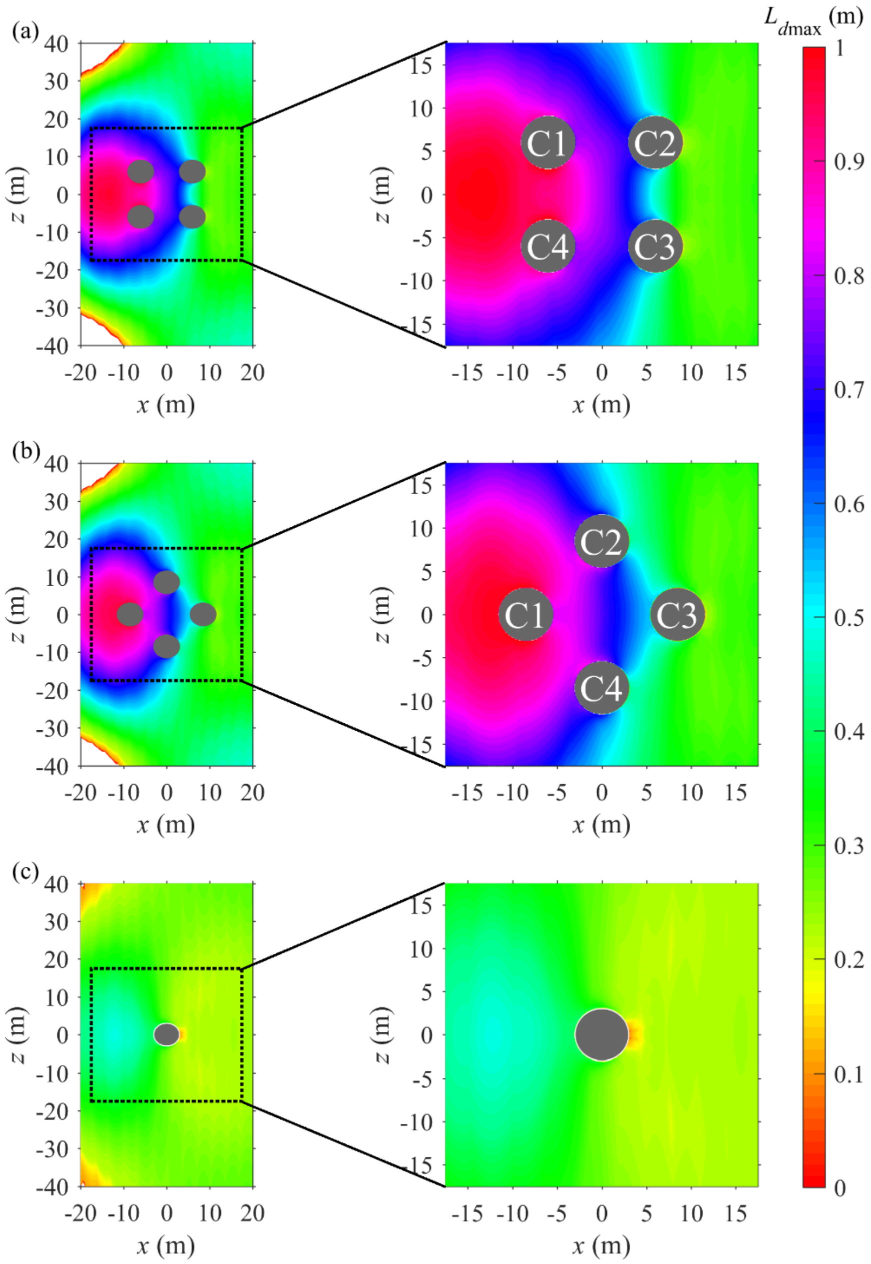

Figure 20 Spatial distribution of the maximum liquefaction depth with (a) 0° incident wave, (b) 45° incident wave, and (c) a mono-pile foundation.

As before, spatial distributions of liquefaction depth are compared with the spatial distribution of the normalized the minimum wave-induced pressure on seabed surface and free surface elevation shown in Figure 21. Spatial distributions of liquefaction depth and the seabed pressure are almost identical, whereas the spatial distribution of the minimum free surface elevation is similar to them, especially in the region near the front cylinders, but also contains higher order harmonics absent from other two. In addition, the normalized minimum wave-induced pressure on seabed surface shown in Figure 21(a), indicates that the approximate range of the amplification factor, resulting from near-trapping phenomenon of incoming wave within a cylinder array, is from 1.1 to 1.4. With shorter incident wave (Case 5 with $k_w D$ = 0.43), the near-trapping effect tends to be more significant, with greater amplification factor, while the liquefaction depth, compared to longer wave (Case 1 with $k_w D$ = 0.35 and L_d of roughly 1.38m), is smaller, roughly 1m, due to the smaller magnitude of wave-induced pressure under wave trough. Nevertheless, the soil response near a cylinder array under such shorter waves should still be examined in terms of liquefaction potential, especially for cylinder arrays where the near-trapping phenomenon is capable of reducing the minimum wave-generated pressure at seabed, compared to a single cylinder.

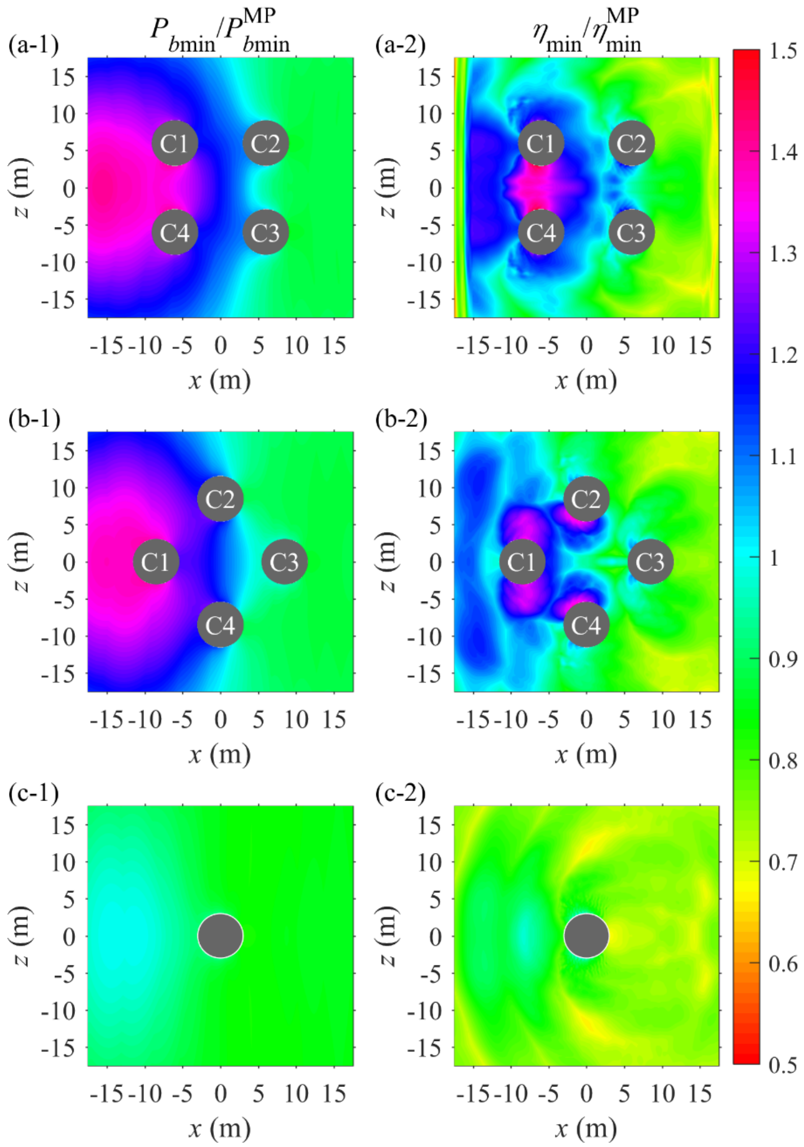

Figure 21 Spatial distribution of the normalized minimum wave-induced pressure ($P_{b\min}$; see subplots a-1, b-1, c-1) on seabed surface and free surface elevation ($\eta_{\min}$; see subplots a-2, b-2, c-2) in a wave period. (a) 0° incident wave; (b) 45° incident wave; (c) a mono-pile foundation.

5. Conclusions

Previous study (Lin et al., 2017) demonstrated that the presence of mono-pile foundation has significant effect on the distribution of wave-induced pore water pressures and associated potential liquefaction. Nevertheless, the understanding of the liquefaction potential around a cylinder array under storm wave remains an unsolved issue. With the WSSI model proposed in Lin et al. (2017), an investigation of wave-induced seabed response and liquefaction potential in the vicinity of closely placed four cylinders has been carried out, for two incident wave angles, namely 0° and 45°, and for a range of wave conditions. The following conclusions can be drawn from this study:

(1) The capability of present wave model to simulate wave-cylinders interaction has been demonstrated. It shows that good accuracy can be obtained, even for higher order components, and for the steep wave. This agrees with the conclusion drawn in Sun et al. (2016) for single cylinder case. This study extends this conclusion to cylinder arrays. The near-trapping phenomenon is well captured and the wave sub-model in the coupled WSSI model is capable of simulating wave-cylinders interaction.

(2) The magnitudes of wave-induced free surface elevation and pressure in the vicinity of a cylinder array, as well as associated liquefaction depth, are amplified by the near-trapping phenomenon occurring during interaction of wave with an array of cylinders. Compared with the results of a mono-pile foundation case under same wave parameters, the amplification factor for liquefaction depth, wave-induced pressure, and free surface elevation is approximately in the range from 1.05 to 1.2. In general, the amplification factor decreases with the increase of wave period. This is also demonstrated in Cong et al. (2015) by experimental and numerical investigations of free surface elevation. Although the numerical results of soil model are highly sensitive to the soil parameters used in the study, the overall phenomenon of soil response under near-trapping effects can still be captured as wave-induced pore pressures within the seabed are well predicted numerically and irrelevant to soil parameters. The potential for liquefaction needs to be examined even in the case with shorter wave and smaller wave height, in which no liquefaction takes place around the mono-pile foundation, but may still happen near a cylinder array, due to the effect of near-trapping phenomenon.

(3) The overall liquefaction depth near a four-cylinder group under 0° incident wave is greater than that under 45° incident wave. This is because the wave with 0° incident direction has significant near-trapping phenomenon inside the cylinder array, which leads to smaller seabed pore pressure than for 45° incident wave. As a result, the porous seabed at the inner zone of a four-cylinder array is more vulnerable to liquefaction threat than that at the outer zone in both incident wave directions since lower wave-induced pressures occur in this zone. Non-symmetric spatial distributions of wave-induced pressure, liquefaction depth, and the minimum free surface elevation are found under 0° wave heading, while those under 45° wave heading are symmetric.

(4) In a four-cylinder array, upstream cylinders provide good protection from momentary liquefaction for downstream cylinders. As before, this directly corresponds to the spatial distribution of the minimum wave-induced pressure on seabed around cylinders. Furthermore, the momentary liquefaction depth is largest at the lateral sides of each cylinder. Good protection from momentary liquefaction therefore needs to be placed in these zones.

Acknowledgement

The authors would like to acknowledge the financial support from Energy Technology Partnership (ETP), Wood Group Kenny, and University of Aberdeen. Zaibin Lin greatly appreciates the helpful discussion with Dr Dominic van der A from the University of Aberdeen. The constructive comments from Prof. Dong-Sheng Jeng at Griffith University have greatly improved the quality of the manuscript.

Nomenclature

A	Wave amplitude	[m]
D	Diameter of pipeline or cylinder	[m]
e	Penetration depth	[m]
E	Young's modulus	[MPa]
$\mathbf{g}$	Gravitational acceleration vector	[m/s^2]
G	Shear modulus of soil	[N/m^2]
h_s	Soil depth	[m]
h_w	Mean water level or water depth	[m]
H_w	Wave height	[m]
k_s	Darcy's permeability	[m/s]
k_w	Wave number	[m^{-1}]
K_0	Coefficient of earth pressure at rest	[-]
K_w	True bulk modulus of elasticity of water	[N/m^2]
L_d	Liquefaction depth	[m]
$L_{d\max}^{\mathrm{MP}}$	The maximum liquefaction depth of a mono-pile foundation	[m]
L_s	Soil domain length	[m]
L_w	Wave length	[m]
$\boldsymbol{n}$	The normal to the body surface	[-]
n_s	Porosity of soil	[-]
p	Total pressure	[kPa]
$P_{b\min}^{\mathrm{MP}}$	The minimum pore water pressure on the seabed surface in a mono-pile foundation case	[kPa]

p_p	Pore water pressure	[kPa]
p_w	Hydrostatic water pressure	[kPa]
P_0	The maximum pore water pressure	[kPa]
P_b	Pore water pressure on the seabed surface	[kPa]
P_{w0}	Absolute pore water pressure	[kPa]
S_r	Saturation degree of soil	[-]
t	Time	[s]
T	Wave period	[s]
$\boldsymbol{u}$	Velocity field	[m/s]
$\boldsymbol{u}_a$	Air velocity	[m/s]
$\boldsymbol{u}_r$	Relative velocity field	[m/s]
$\boldsymbol{u}^{\mathrm{T}}$	Transpose matrix of velocity field	[m/s]
$\boldsymbol{u}_w$	Water velocity	[m/s]
$\boldsymbol{v}$	$\boldsymbol{v} = (u_s, v_s, w_s)$, the vector of soil displacement	[m]
$\boldsymbol{x}$	$\boldsymbol{x} = (x, y, z)$, Cartesian coordinate vector where y is the vertical coordinate, x and z are the horizontal coordinates.	[m]
W_s	Soil domain width	[m]
α	Volume fraction function	[-]
β_s	Compressibility of pore fluid	[m^2/N]
γ_s	Unit weight of soil	[kN/m^3]
γ_w	Unit weight of water	[kN/m^3]
ε_s	Volume strain	[-]
η	Free surface elevation	[m]
$\eta_{\min}$	The minimum free surface elevation	[m]
$\eta_{\min}^{\mathrm{MP}}$	The minimum free surface elevation in the mono-pile case	[m]
θ	Angle along circular cylinder circumference	[°]
θ_w	Wave direction	[°]

μ	Dynamic viscosity	[kg/sm]
μ_w	Dynamic viscosity of water	[kg/sm]
μ_a	Dynamic viscosity of air	[kg/sm]
ν	Poisson's ratio	[-]
ρ	Fluid density	[kg/m^3]
ρ_w	Water density	[kg/m^3]
ρ_a	Air density	[kg/m^3]
σ_{ij}	The rate of the strain tensor	[-]
σ'	Effective normal stress	[kPa]
τ	Shear stress	[kPa]
ω	Frequency of incident wave	[s^{-1}]

References

Berberović, E., van Hinsberg, N.P., Jakirlić, S., Roisman, I.V. and Tropea, C., 2009. Drop impact onto a liquid layer of finite thickness: Dynamics of the cavity evolution. *Physical Review E*, 79(3): 036306.

Bihs, H., Kamath, A., Alagan Chella, M. and Arntsen, Ø.A., 2016. Breaking-Wave Interaction with Tandem Cylinders under Different Impact Scenarios. *Journal of Waterway, Port, Coastal, and Ocean Engineering, ASCE*: 04016005.

Biot, M.A., 1941. General theory of three-dimensional consolidation. *Journal of Applied Physics*, 12(2): 155-164.

Chang, K.-T. and Jeng, D.-S., 2014. Numerical study for wave-induced seabed response around offshore wind turbine foundation in Donghai offshore wind farm, Shanghai, China. *Ocean Engineering*, 85: 32-43.

Chen, L., Zang, J., Hillis, A., Morgan, G. and Plummer, A., 2014. Numerical investigation of wave–structure interaction using OpenFOAM. *Ocean Engineering*, 88: 91-109.

Cong, P., Gou, Y., Teng, B., Zhang, K. and Huang, Y., 2015. Model experiments on wave elevation around a four-cylinder structure. *Ocean Engineering*, 96: 40-55.

Duan, L. and Jeng, D.-S., 2018. Numerical studies for wave-induced pore-water pressures around group of piled foundations. *The 28th ISOPE International Ocean and Polar Engineering Conference*, Sapporo, Hokkaido, Japan, June 10-15, 2018 (CD-ROM).

Duan, L., Jeng, D.S. and Wang, D., 2019. PORO-FSSI-FOAM: Seabed response around a mono-pile under natural loadings. *Ocean Engineering*, 184: 239-254.

Engsig-Karup, A.P., Bingham, H.B. and Lindberg, O., 2009. An efficient flexible-order model for

3D nonlinear water waves. *Journal of computational physics*, 228(6): 2100-2118.

Higuera, P., Lara, J.L. and Losada, I.J., 2013a. Realistic wave generation and active wave absorption for Navier–Stokes models: Application to OpenFOAM®. *Coastal Engineering*, 71: 102-118.

Higuera, P., Lara, J.L. and Losada, I.J., 2013b. Simulating coastal engineering processes with OpenFOAM®. *Coastal Engineering*, 71: 119-134.

Higuera, P., Lara, J.L. and Losada, I.J., 2014a. Three-dimensional interaction of waves and porous coastal structures using OpenFOAM®. Part I: Formulation and validation. *Coastal Engineering*, 83: 243-258.

Higuera, P., Lara, J.L. and Losada, I.J., 2014b. Three-dimensional interaction of waves and porous coastal structures using OpenFOAM®. Part II: Application. *Coastal Engineering*, 83: 259-270.

Higuera, P., Losada, I.J. and Lara, J.L., 2015. Three-dimensional numerical wave generation with moving boundaries. *Coastal Engineering*, 101: 35-47.

Hirt, C.W. and Nichols, B.D., 1981. Volume of fluid (VOF) method for the dynamics of free boundaries. *Journal of computational physics*, 39(1): 201-225.

Jacobsen, N.G., Fuhrman, D.R. and Fredsøe, J., 2012. A wave generation toolbox for the open-source CFD library: OpenFoam®. *International Journal for Numerical Methods in Fluids*, 70(9): 1073-1088.

Jeng, D.-S., 2003. Wave-induced sea floor dynamics. *Applied Mechanics Reviews*, 56(4): 407-429.

Jeng, D.-S., 2013. Porous Models for Wave-seabed Interactions. *Springer Berlin Heidelberg*.

Jeng, D.-S. and Cha, D.H., 2003. Effects of dynamic soil behavior and wave non-linearity on the wave-induced pore pressure and effective stresses in porous seabed. *Ocean Engineering*, 30(16): 2065-2089.

Jeng, D.-S., Ye, J.H., Zhang, J.S. and Liu, P.L.F., 2013. An integrated model for the wave-induced seabed response around marine structures: Model verifications and applications. *Coastal Engineering*, 72(0): 1-19.

Jeng, D.S., 2018. Mechanics of Wave-seabed-structure Interactions: Modelling, Processes and Applications. *Cambridge University Press*.

Kamath, A., Bihs, H., Alagan Chella, M. and Arntsen, Ø.A., 2016. Upstream-cylinder and downstream-cylinder influence on the hydrodynamics of a four-cylinder group. *Journal of Waterway, Port, Coastal, and Ocean Engineering, ASCE*: 04016002.

Kamath, A., Chella, M.A., Bihs, H. and Arntsen, Ø.A., 2015. CFD investigations of wave interaction with a pair of large tandem cylinders. *Ocean Engineering*, 108: 738-748.

Kirby, J., Wen, L. and Shi, F., 2003. Funwave 2.0 fully nonlinear boussinesq wave model on curvilinear coordinates. *Center for Applied Coastal Research Dept. of Civil & Environmental Engineering, University of Delaware, Newark*.

Li, X.-J., Gao, F.-P., Yang, B. and Zang, J., 2011. Wave-induced pore pressure responses and soil liquefaction around pile foundation. *International Journal of Offshore and Polar Engineering*, 21(03).

Li, Y., Ong, M.C. and Tang, T., 2018. Numerical analysis of wave-induced poro-elastic seabed response around a hexagonal gravity-based offshore foundation. *Coastal Engineering*, 136: 81-95.

Liao, C., Jeng, D.-S. and Zhang, L., 2013. An analytical approximation for dynamic soil response of a porous seabed due to combined wave and current loading. *Journal of Coastal Research*, 31(5): 1120-1128.

Lin, Z., Guo, Y., Jeng, D.-S., Liao, C. and Rey, N., 2016. An integrated numerical model for wave–soil–pipeline interactions. *Coastal Engineering*, 108: 25-35.

Lin, Z., Pokrajac, D., Guo, Y., Jeng, D.-S., Tang, T., Rey, N., Zheng, J. and Zhang, J., 2017. Investigation of nonlinear wave-induced seabed response around mono-pile foundation. *Coastal Engineering*, 121: 197-211.

Linton, C. and Evans, D., 1990. The interaction of waves with arrays of vertical circular cylinders. *Journal of fluid mechanics*, 215: 549-569.

Liu, B., Jeng, D.-S., Ye, G. and Yang, B., 2015. Laboratory study for pore pressures in sandy deposit under wave loading. *Ocean Engineering*, 106: 207-219.

Liu, X., García, M.H. and Muscari, R., 2007. Numerical investigation of seabed response under waves with free-surface water flow. *International Journal of Offshore and Polar Engineering*, 17(02).

Malenica, Š., Eatock Taylor, R. and Huang, J., 1999. Second-order water wave diffraction by an array of vertical cylinders. *Journal of Fluid Mechanics*, 390: 349-373.

Ohl, C., Eatock Taylor, R., Taylor, P. and Borthwick, A., 2001a. Water wave diffraction by a cylinder array. Part 1. Regular waves. *Journal of Fluid Mechanics*, 442: 1-32.

Ohl, C., Taylor, P., Eatock Taylor, R. and Borthwick, A., 2001b. Water wave diffraction by a cylinder array. Part 2. Irregular waves. *Journal of Fluid Mechanics*, 442: 33-66.

Paulsen, B.T., Bredmose, H. and Bingham, H.B., 2014a. An efficient domain decomposition strategy for wave loads on surface piercing circular cylinders. *Coastal Engineering*, 86: 57-76.

Paulsen, B.T., Bredmose, H., Bingham, H.B. and Jacobsen, N.G., 2014b. Forcing of a bottom-mounted circular cylinder by steep regular water waves at finite depth. *Journal of Fluid Mechanics*, 755: 1-34.

Qi, W.-G. and Gao, F.-P., 2014. Physical modeling of local scour development around a large-diameter monopile in combined waves and current. *Coastal Engineering*, 83: 72-81.

Shi, F., Dalrymple, R.A., Kirby, J.T., Chen, Q. and Kennedy, A., 2001. A fully nonlinear Boussinesq model in generalized curvilinear coordinates. *Coastal Engineering*, 42(4): 337-358.

Spring, B.H. and Monkmeyer, P.L., 1974. Interaction of plane waves with vertical cylinders. *Proceedings of the 14th international conference on coastal engineering*.

Sui, T., Zhang, C., Guo, Y., Zheng, J., Jeng, D.-S., Zhang, J. and Zhang, W., 2016. Three-dimensional numerical model for wave-induced seabed response around mono-pile. *Ships and Offshore Structures*: 1-12.

Sui, T., Zheng, J., Zhang, C., Jeng, D.-S., Zhang, J., Guo, Y. and He, R., 2017. Consolidation of unsaturated seabed around an inserted pile foundation and its effects on the wave-induced momentary liquefaction. *Ocean Engineering*, 131: 308-321.

Sui, T.T., Zhang, C., Jeng, D.S., Guo, Y.K., Zheng, J.H., Zhang, W. and Shi, J. 2019. Wave-induced seabed residual response and liquefaction around a monopile foundation with various embedded depth. ***Ocean Engineering***, 173: 157-173.

Sumer, B.M., 2014. Liquefaction Around Marine Structures. *World scientific, New Jersey*.

Sumer, B.M. and Fredsøe, J., 2002. The mechanics of scour in the marine environment. *World Scientific, New Jersey*.

Sun, K., Zhang, J.S., Gao, Y., Jeng, D.S., Guo, Y.K. and Liang, Z.D. 2019. Laboratory experimental study of ocean waves propagating over a partially buried pipeline in a trench layer. ***Ocean Engineering***, 173: 617-627.Sun, L., Zang, J., Chen, L., Eatock Taylor, R. and Taylor, P., 2016. Regular waves onto a truncated circular column: A comparison of experiments and simulations. *Applied Ocean Research*, 59: 650-662.

Tang, T., 2014. Modeling of soil-water-structure interaction: A Finite Volume Method (FVM) approach to fully coupled soil analysis and interactions between wave, seabed and offshore structure. PhD thesis, Technical University of Denmark.

Tang, T. and Hededal, O., 2014. Simulation of pore pressure accumulation under cyclic loading using Finite Volume Method. *Proceedings of 8th European Conference on Numerical Methods in Geotechnical Engineering (numge14)*.

Tang, T., Hededal, O. and Cardiff, P., 2015. On finite volume method implementation of poro-elasto-plasticity soil model. *International Journal for Numerical and Analytical Methods in Geomechanics*, 39(13): 1410-1430.

Tong, D., Liao, C. and Chen, J., 2019. Wave-monopile-seabed interaction considering nonlinear pile-soil contact. *Computers and Geotechnics*, 113: 103076.

Tong, D., Liao, C., Jeng, D.-S., Zhang, L., Wang, J. and Chen, L., 2017. Three-dimensional modeling of wave-structure-seabed interaction around twin-pile group. *Ocean Engineering*, 145: 416-429.

Tonkin, S., Yeh, H., Kato, F. and Sato, S., 2003. Tsunami scour around a cylinder. *Journal of Fluid Mechanics*, 496: 165-192.

Tuković, Ž., Cardiff, P., Karac, A., Jasak, H. and Ivankovic, A., 2014. OpenFOAM Library for Fluid Structure Interaction. *9th International OpenFOAM® Workshop*.

Twersky, V., 1952. Multiple scattering of radiation by an arbitrary configuration of parallel cylinders. *The Journal of the Acoustical Society of America*, 24(1): 42-46.

Ulker, M. and Rahman, M., 2009. Response of saturated and nearly saturated porous media: Different formulations and their applicability. *International journal for numerical and analytical methods in geomechanics*, 33(5): 633-664.

Ulker, M.B.C., Rahman, M.S. and Jeng, D.-S., 2009. Wave-induced response of seabed: various formulations and their applicability. *Applied Ocean Research*, 31(1): 12-24.

Wei, G., Kirby, J.T. and Sinha, A., 1999. Generation of waves in Boussinesq models using a source function method. *Coastal Engineering*, 36(4): 271-299.

Ye, J., Jeng, D.-S., Chan, A., Wang, R. and Zhu, Q., 2016. 3D Integrated numerical model for fluid–structures–seabed interaction (FSSI): Elastic dense seabed foundation. *Ocean Engineering*, 115: 107-122.

Ye, J., Jeng, D.-S., Wang, R. and Zhu, C., 2013. A 3-D semi-coupled numerical model for fluid–structures–seabed-interaction (FSSI-CAS 3D): Model and verification. *Journal of Fluids and Structures*, 40: 148-162.

Zhang, J., Sun, K., Zhai, Y., Zhang, H. and Zhang, C., 2016. Physical Study on Interactions between Waves and a Well-mixed Seabed. *Journal of Coastal Research*: 198-203.

Zhang, J.S., Jeng, D.-S. and Liu, P.L.F., 2011. Numerical study for waves propagating over a porous seabed around a submerged permeable breakwater: PORO-WSSI II model. *Ocean Engineering*, 38(7): 954-966.

Zhang, Q., Zhou, X.-L., Wang, J.-H. and Guo, J.-J., 2017. Wave-induced seabed response around an offshore pile foundation platform. *Ocean Engineering*, 130: 567-582.

Zhao, H.Y. and Jeng, D.-S., 2016. Accumulated Pore Pressures around Submarine Pipeline Buried in Trench Layer with Partial Backfills. *Journal of Engineering Mechanics, ASCE*: 04016042.

Zhao, H.Y., Jeng, D.S., Liao, C.C. and Zhu, J.F., 2017. Three-dimensional modeling of wave-induced residual seabed response around a mono-pile foundation. *Coastal Engineering*, 128: 1-21.